

XMM-NEWTON ARCHIVAL STUDY OF THE ULTRALUMINOUS X-RAY POPULATION IN NEARBY GALAXIES

LISA M. WINTER

Astronomy Department, University of Maryland, College Park, MD 20742; lwinter@astro.umd.edu

RICHARD F. MUSHOTZKY

NASA Goddard Space Flight Center, Greenbelt, MD 20771; richard@milkyway.gsfc.nasa.gov

AND

CHRISTOPHER S. REYNOLDS

Astronomy Department, University of Maryland, College Park, MD 20742; chris@astro.umd.edu

Received 2005 March 10; accepted 2006 May 30

ABSTRACT

We present the results of an archival *XMM-Newton* study of the bright X-ray point sources ($L_X > 10^{38}$ ergs s^{-1}) in 32 nearby galaxies. From our list of approximately 100 point sources, we attempt to determine if there is a low-state counterpart to the ultraluminous X-ray (ULX) population, searching for a soft-hard state dichotomy similar to that known for Galactic X-ray binaries and testing the specific predictions of the intermediate-mass black hole (IMBH) hypothesis. To this end, we searched for “low-state” objects, which we defined as objects within our sample that had a spectrum well fitted by a simple absorbed power law, and “high-state” objects, which we defined as objects better fitted by a combined blackbody and a power law. Assuming that low-state objects accrete at approximately 10% of the Eddington luminosity (as found by Done & Gierlinski) and that high-state objects accrete near the Eddington luminosity, we further divided our sample of sources into low- and high-state ULX sources. We classify 16 sources as low-state ULXs and 26 objects as high-state ULXs. As in Galactic BH systems, the spectral indices, Γ , of the low-state objects, as well as the luminosities, tend to be lower than those of the high-state objects. The observed range of blackbody temperatures for the high state is 0.1–1 keV, with the most luminous systems tending toward the lowest temperatures. We therefore divide our high-state ULXs into candidate IMBHs (with blackbody temperatures of approximately 0.1 keV) and candidate stellar mass BHs (with blackbody temperatures of approximately 1.0 keV). A subset of the candidate stellar mass BHs have spectra that are well fitted by a Comptonization model, a property similar to Galactic BHs radiating in the “very high” state near the Eddington limit.

Subject headings: accretion, accretion disks — galaxies: general — surveys — X-rays: binaries

Online material: machine-readable table

1. INTRODUCTION

Through X-ray observations of nearby galaxies, a class of ultraluminous X-ray (ULX) sources has emerged. These are pointlike, nonnuclear sources with observed X-ray luminosities greater than 10^{39} ergs s^{-1} (Miller & Colbert 2004). Of most interest are those sources with bolometric luminosities in excess of the Eddington limit for a $20 M_\odot$ black hole (BH), or $L_{\text{bol}} > 2.8 \times 10^{39}$ ergs s^{-1} . The true nature of these sources is unclear, and this class most likely includes several different types of objects. Although some of these sources are located within a few parsecs of their host galaxy’s dynamical center, they do not exhibit many of the characteristics of active galactic nuclei (AGNs). Because the ratio of X-ray to optical flux is a factor of 10 greater than that of AGNs (Anderson et al. 2003; Stocke et al. 1983), these objects are fairly easy to recognize in X-ray imaging data.

Assuming that the Eddington limit is obeyed by BH accretion, the existence of such luminous non-AGN sources presents a puzzle. Several models have been proposed to account for the high luminosities of the ULXs. Among these are relativistic and non-relativistic beaming from stellar mass BH systems (Reynolds et al. 1997; King et al. 2001; Kording et al. 2002) and accretion of matter into intermediate-mass black holes (IMBHs). In several ULX systems (NGC 1313 X-2, M81 X-9, etc.), detection of emission nebulae surrounding the ULX supports isotropic emis-

sion from the central source (Pakull & Mirioni 2003), which cannot be described through beaming. Further, a number of ULX (NGC 1313 X-1, etc.) X-ray spectra are best fitted with combined multicomponent blackbody disk model (MCD) and power-law fits, similar to Galactic BHs in their high state. Recently, Miller et al. (2004) found that many spectral fits of ULXs require cool accretion disk temperatures of approximately 100 eV. The theoretical relationship between BH mass and disk temperature ($T \propto M^{-1/4}$) has been observed to hold true for stellar mass (typically around 1 keV) and supermassive (around 10–100 eV) BHs (Makishima et al. 2000; Porquet et al. 2004; Gierliński & Done 2004). Using these scaling relations, the cool accretion disk ULXs would correspond to a population of high-state IMBHs with masses of $\approx 16\text{--}10^4 M_\odot$.

If ULXs do not obey the Eddington limit, they could be the result of an outburst (such as can occur in low-mass X-ray binaries within our own Galaxy). Jonker & Nelemans (2004) find evidence for approximately five Galactic BH X-ray binaries that exhibit luminosities in the ULX range during outbursts. These sources would appear as transient ULXs. The typical timescale for outburst of Galactic X-ray transients is a few days to rise from quiescent level with a decline from peak brightness to quiescent value of 30–40 days (Chen et al. 1997). Another possible explanation is super-Eddington emission from accretion disks surrounding stellar mass BHs (Begelman 2002; Ebisawa et al. 2003).

Sources of this type would be expected to have soft X-ray components well modeled by hot accretion disks ($\approx 1.3\text{--}2.0$ keV) similar to superluminal X-ray sources in the Galaxy (e.g., Belloni et al. 1997).

Likely, ULXs include a variety of different objects with both isotropic and nonisotropic emitters. However, if some ULXs do indeed represent a class of high-state IMBHs, similar to the high/soft (thermal dominated) state stellar mass BHs in our Galaxy, we might also expect to see the low-state objects from this same population. In Galactic BH systems, the low state is generally characterized by lower luminosity, with $L < 0.1L_{\text{Edd}}$ (Done & Gierlinski 2003), and a power-law photon spectrum, typically with index $\Gamma \approx 1.7$ (Remillard & McClintock 2006). Indeed, the existence of some ULX sources (IC 342 X-1, NGC 5204 X-1) as possible low-hard (pure power law) state IMBHs, well fitted by simple absorbed power laws, has been noted from *Chandra* observations by Roberts et al. (2004). In this study we seek to test a direct prediction of the IMBH hypothesis, namely, whether there is a class of sources with properties consistent with what we expect of low-state IMBHs. This requires two major assumptions: (1) that the emission from ULXs is isotropic and (2) that IMBHs exhibit the same states (whose classification was based on luminosity and spectral form) as stellar mass BHs. Our goal is to find these “low-state” sources, if they exist, classify the properties of both high-state and low-state ULXs, and test whether these data are consistent or inconsistent with the predictions of the IMBH hypothesis.

We present the results of a detailed analysis of ULXs in nearby galaxies observed with the European Space Agency’s *XMM-Newton* observatory. Only *XMM-Newton* provides the count rates and bandpass necessary to distinguish different spectral models for most ULXs, accurately determine the temperature of the thermal component expected for high-state objects, and determine whether this component is required in the spectral modeling of these objects. Since the *XMM-Newton* X-ray spectra of ULXs are similar in quality to spectra for Galactic X-ray binaries obtained in the 1980s, our spectral classification in this paper remains purely schematic. Thus, our classifications as low- and high-state objects are a first approximation, based on the quality of the spectra available.

In § 2 we detail the observations examined from the *XMM-Newton* archives and explain the data analysis for the individual point sources. In § 3 we discuss the spectral fitting technique, as well as simulations we conducted to determine their validity. We discuss the implications of our results in § 4.

2. OBSERVATIONS AND DATA REDUCTION

The data used in this investigation were drawn from the *XMM-Newton* public data archive. Assuming that low-state ULXs exist in the luminosity range of $10^{38}\text{--}10^{39}$ ergs s^{-1} , we conducted simulations to determine the optimum criteria for observations capable of resolving point sources of this luminosity. Our simulations provided a guide for choosing which of the vast number of archival *XMM-Newton* data sets we should examine. This luminosity range was chosen on the assumption that an approximately $100 M_{\odot}$ BH would radiate at $\approx 10\%$ of the L_{Edd} in the low state (Done & Gierlinski 2003).

Within the luminosity range of interest ($L_X > 10^{38}$ ergs s^{-1}), there are a number of known objects that could be confused with ULX sources. One type of source is supernova remnants (SNRs). These sources are often easy to distinguish based on their characteristic spectrum: with poor signal-to-noise ratio (S/N) we expect a steep power law, and as the S/N increases, emission lines become clearly visible. Super-Eddington accreting neutron stars

(NSs) have been observed to have luminosities within this range for a short period of time. NS X-ray binaries often have spectra well fitted by a hot multicolor disk blackbody model or, with low S/N, by a bremsstrahlung model. Both models have similar curvature, and a $0.7\text{--}2.0$ keV blackbody model is indistinguishable from the bremsstrahlung model. We chose to use the bremsstrahlung model because it is the simpler model and gives an adequate qualitative description of the data. We expect that for low-temperature bremsstrahlung sources, the spectrum should be easily distinguishable from a power law with $\Gamma \approx 1.7$ (as is expected for a low-state object). If, however, the NS spectrum has $kT > 5$ keV, as observed for some NS X-ray binaries, our simulations show that we cannot distinguish between the power-law and bremsstrahlung models.

The most common sources we expected to find in this luminosity range were the analogs to Galactic BH X-ray binaries in their high-soft (thermal dominated) state. These sources typically have spectra well fitted by a blackbody with temperature of ≈ 1.0 keV combined with a power law with index $\Gamma \approx 2.5$. Our simulations sought to determine the number of photons required to distinguish between spectral fits corresponding to a power-law model with $\Gamma \approx 1.7$ and a combined blackbody and power-law model. These models qualitatively correspond to those of a low-state (pure power-law spectrum) and high-state (thermal-dominated spectrum) X-ray binary. Since we do not know the proper normalization between the blackbody and power-law components for high-state objects (it varies from source to source), we tested whether each of the components separately, e.g., blackbody or a steep power law, could be distinguished from the simulated low-state spectrum. We chose to simulate spectra in XSPEC using the command `fakeitnone`. We used generic response and ancillary response matrices. Simulating a power-law model with a $\Gamma = 1.7$, we found that for 200, 400, and 1000 counts these models were distinguishable at $>99\%$ confidence from a blackbody source (with kT constrained to the range of $0.6\text{--}1.3$ keV, similar to that of Galactic BHs). We found that for a lower number of counts the distribution in Γ -values increases to include a larger range of Γ -values (i.e., $\Gamma = 1.3\text{--}2.0$ compared to $\Gamma = 1.5\text{--}1.7$). Simulating a power law with $\Gamma = 2.5$, we find the same trend. We determined that at roughly 400 counts the distributions of Γ from a $\Gamma = 1.7$ and $\Gamma = 2.5$ power law become entirely separable at $>99\%$ confidence.

In order to distinguish between the different spectral fits for objects with $L_X \sim 2 \times 10^{38}$ ergs s^{-1} , we select all galaxies that were observed for at least 10 ks (with the exception of the bright ULX in NGC 5408, which had enough photons for analysis despite the low exposure time) with *XMM-Newton* and that are closer than 8 Mpc. We estimated that these criteria would give us a minimum of 400 counts for objects with $L_X > 2 \times 10^{38}$ ergs s^{-1} . We emphasize that the criteria quoted, based on the simulations, were used as a guide in choosing the sample of galaxies examined in this study. These simulations are not used as the statistical basis for our object-by-object analysis (discussed in § 3).

Our sample of galaxies is selective in that it represents objects of interest in the X-ray band. We include details on these host galaxies in Table 1. *XMM-Newton* spectral information of individual X-ray sources had previously been published for approximately 60% of the host galaxies. We include references in the alternate ID column and footnotes of Table 6. We do not compare our results with these previous studies on a source-by-source basis.

We found that abstracts describing the proposals for *XMM-Newton* observations were available for only 13 of the 32 galaxies examined. Of these 13, only one observation cited the motive

TABLE 1
XMM-Newton GALAXY OBSERVATIONS

| Galaxy | Type ^a | n_{H}^{b} (10^{20} cm^{-2}) | Distance ^c (Mpc) | References | ObsID ^d | Duration (s) | Comments |
|------------------|-------------------|--|--------------------------------|------------|------------------------|-----------------|------------------------------|
| NGC 247..... | SAB(s)d | 1.54 | 3.09 | | 0110990301 | 14536 | |
| NGC 253..... | SAB(s)c; H II | 1.40 | 3.73 | | 0110900101, 0152020101 | 30711, 110591 | Starburst |
| NGC 300..... | SA(s)d | 3.11 | 2.56 | | 0112800101 | 43967 | |
| NGC 625..... | SB(s)m? sp; H II | 2.15 | 2.62 | | 0085100101 | 26288 | |
| NGC 1313..... | SB(s)d; H II | 4.0 | 4.17 | | 0106860101 | 41310 | |
| IC 0342..... | SAB(rs)cd; H II | 30.3 | 3.9 | 1 | 0093640901 | 11217 | |
| NGC 1569..... | IBm | 21.7 | 1.6 | 1 | 0112290801 | 15582 | Starburst |
| NGC 1705..... | SA0- pec; H II | 3.9 | 5.1 | 2 | 0148650101 | 58926 | Starburst |
| Mrk 71..... | BCD; H II | 3.9 | 3.4 | 3 | 0141150201 | 45919 | Galaxy pair |
| NGC 2403..... | SAB(s)cd; H II | 4.15 | 3.56 | | 0150651201 | 11415 | |
| Holmberg II..... | Im | 3.42 | 2.70 | | 0112520701, 0112520901 | 13528, 6860 | |
| Holmberg I..... | IAB(s)m | 3.49 | 3.6 | 4 | 0026340101 | 26280 | |
| M81..... | SA(s)ab; LINER | 4.12 | 3.6 | 4 | 0111800101 | 127913 | Hol IX also in field of view |
| M82..... | I0; H II | 4.14 | 3.9 | 5 | 0112290201 | 29387 | Starburst |
| Holmberg IX..... | Im | 4.0 | 3.6 | 4 | 0112521001 | 10350 | M81 also in field of view |
| Sextans A..... | IBm | 3.85 | 1.4 | 6 | 0026340201 | 21618 | |
| IC 2574..... | SAB(s)m | 2.29 | 3.6 | 7 | 0026340301 | 24263 | Bursting star formation |
| NGC 4214..... | IAB(s)m; H II | 1.49 | 2.7 | | 0035940201 | 14744 | |
| NGC 4258..... | SAB(s)bc; LINER | 1.2 | 7.2 | | 0059140901, 0110920101 | 16146, 21895 | |
| NGC 4395..... | SA(s)m; LINER | 1.33 | 4 | | 0112521901 | 15842 | |
| NGC 4449..... | IBm; H II | 1.39 | 3.08 | | 0112521701 | 15522 | |
| NGC 4490..... | SB(s)d | 1.78 | 7.8 | 1 | 0112280201 | 17754 | Interacting with NGC 4485 |
| NGC 4631..... | SB(s)d | 1.28 | 7.5 | 1 | 0110900201 | 53850 | |
| NGC 4736..... | (R)SA(r)ab; LINER | 1.43 | 4.3 | 1 | 0094360601 | 23461 | |
| NGC 4945..... | SB(s)cd; Sy2 | 15.9 | 3.1 | | 0112310301 | 23062 | |
| NGC 5204..... | SA(s)m; H II | 1.42 | 4.8 | 1 | 0142770101, 0142770301 | 19205, 16387 | |
| M51..... | Sc; Sy2 | 1.55 | 7.2 | 1 | 0112840201 | 20924 | Galaxy pair |
| M83..... | SAB(s)c; H II | 3.94 | 6.2 | | 0110910201 | 30627 | Starburst |
| NGC 5253..... | Im pec; H II | 3.77 | 3.2 | 1 | 0035940301 | 47216 | Starburst |
| M101..... | SAB(rs)cd | 1.17 | 7.4 | 8 | 0104260101 | 43019 | |
| NGC 5408..... | IB(s)m; H II | 5.73 | 4.8 | 9 | 0112290601 | 7757 | |
| Circinus..... | SA(s)b; Sy2 | 57.8 | 4 | 10 | 0111240101 | 110496 | |

^a From the NASA/IPAC Extragalactic Database (NED).

^b Column density, obtained from the Web version of the nH FTOOL.

^c Distance (if no reference is given, obtained from the distance modulus given in LEDA).

^d *XMM-Newton* observation identifications for the data examined in this survey.

REFERENCES.—(1) Tully 1988; (2) Tosi et al. 2001; (3) Tolstoy et al. 1995; (4) Freedman et al. 1994; (5) Sakai & Madore 1999; (6) Sakai et al. 1996; (7) Shapley et al. 2001; (8) Kelson 1996; (9) Karachentsev et al. 2002; (10) Freeman et al. 1977.

as a study of ULXs (NGC 1313). However, 7 of the remaining 19 galaxies contained sources classified as intermediate X-ray objects (IXOs) by Colbert & Ptak (2002). If the remaining galaxies were not studied due to their ULX population, the effects of bias are small with roughly 25% of the sources studied explicitly due to their connection with ULX sources. Our host galaxies include only spiral and irregular galaxies. Figure 1 displays the distribution of galaxy type.

We reduced the data using the *XMM-Newton* Science Analysis System (SAS) version 6.0.0. Since the processed pipeline products (PPS) were created with earlier versions of SAS, the observation data files (ODFs) were used to produce calibrated photon event files for the EPIC MOS and PN cameras using the commands `emchain` and `epchain`. Following this, the events tables were filtered using the standard criteria outlined in the *XMM-Newton* ABC Guide. For the MOS data (both MOS1 and MOS2 cameras), good events constitute those with a pulse height in the range of 0.2–12 keV and event patterns that are characterized as 0–12 (single, double, triple, and quadruple pixel events). For the PN camera, only patterns of 0–4 (single and double pixel events) are kept, with the energy range for the pulse height set between 0.2 and 15 keV. Bad pixels and events too close to the edges of

the CCD chips were rejected using the stringent selection expression “FLAG == 0.”

Time filtering was applied as needed by editing the light curve produced in `xmmselect` for the entire observation. Flare events (distinguished by their high count rate) detected in all three cameras were cut using the `tabgtigen` task as outlined in the ABC Guide. Typical count rate parameters for filtering were “RATE < 5” for MOS detectors and “RATE < 20” for the PN detector. Such filtering was only done as needed. Prefiltered exposure times are listed in Table 1. The number of counts from the filtered net exposure times for the individual sources is listed in Table 6. We note that the filtered data are not always sufficiently clean that a high S/N is maintained up to 10 keV. Sources with a high background flux level, relative to the source spectrum, show poorer S/N in the spectrum above 1 keV.

Before extracting spectra of the brightest sources, contour maps of the X-ray observation were overlaid on Digital Sky Survey (DSS) images. This ensured that bright foreground stars and background AGNs were easily distinguished and thereby not included in our sample. Also, we checked the *XMM-Newton* source positions with NED and SIMBAD to determine if they coincide with any known background galaxies or QSOs. A list

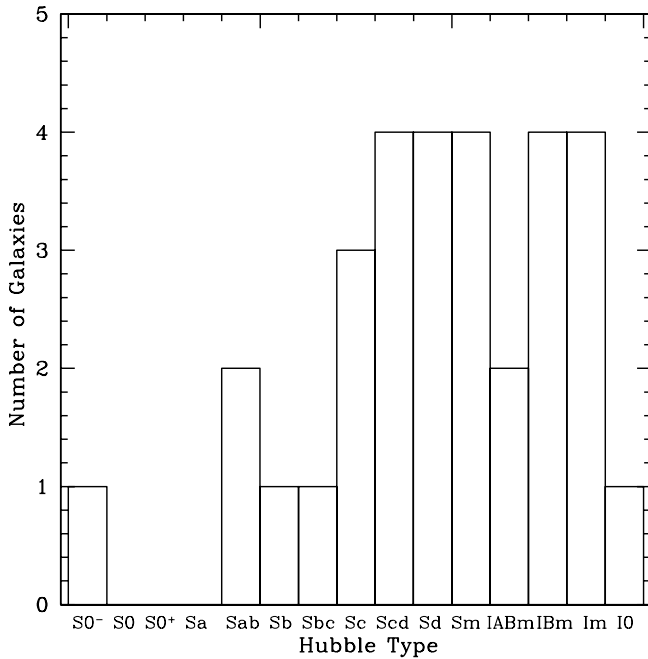


FIG. 1.— Distribution of galaxies by Hubble type among our archival *XMM-Newton* sample of nearby (<8 Mpc) galaxies. Our sample consists solely of spiral and irregular galaxies.

of these bright foreground or background sources is included in Table 7.

3. SPECTRAL FITTING

Spectra for the bright point sources were extracted based on their apparent brightness in the CCD images. No explicit source detection algorithm was necessary. We used the SAS task *especget*. With this task we created spectra (for both the source and background), response matrices, and ancillary response files for all three EPIC cameras, when possible. The typical extraction radius was $20''$, but depending on both the size and proximity of a source to another source, the extraction radius ranged from $9''$ to $87''$. Background spectra were extracted either in an annulus centered on the source or in a circle of appropriate size away from the source, depending on the proximity of the candidate source to other X-ray sources. Annuli were used for sources that were not located within a few arcseconds of another source; thus, annular background extraction radii were not used for sources with small extraction radii. For sources in crowded regions, we used circular extraction radii close to the source. We extracted backgrounds close to the source in order to correct for emission local to the ULX. Once the spectra were obtained, they were rebinned to require at least 20 counts bin^{-1} , using the command *grppha* in LHEASOFT. The list of sources, with position and count information, is included in Table 6. We only included sources for our spectral studies that had 400 or greater PN counts (or MOS for sources in NGC 253, M81, NGC 4945 XMM3, and NGC 2403 XMM1, for which PN spectra were not available).

The extracted spectra were fitted with standard models in XSPEC version 11.3.1. For each source, we fitted the PN and MOS spectra simultaneously in the 0.3–10 keV range. We allowed a free normalization constant to account for the differences in flux calibration between the three cameras (similar to Jenkins et al. 2004). Each source was first fitted with an absorbed single-component model. In all cases we used the standard absorption model *wabs*, leaving the column density as a free parameter.

For those sources where the hydrogen column density was unconstrained, we fixed the value to the Galactic foreground value listed in Table 1.

3.1. Single-Component Sources

Results of the single-component fits are seen in Table 2. We include in this table only the best-fit parameters for those sources best described by a single-component model. The addition of a blackbody component to these single-component fits changes the χ^2 value by a negligible amount and therefore is not statistically significant. More specifically, the addition of a blackbody model to the power-law fit corresponds to a $\Delta\chi^2 < 2.3$, which is the $\approx 68\%$ confidence level using the *F*-test for 2 degrees of freedom.

The flux values quoted represent the unabsorbed flux in the PN spectra, in the 0.3–10 keV band. All errors quoted, here and subsequently, correspond to the 90% confidence level for 1 degree of freedom ($\Delta\chi^2 = 2.71$). The luminosities were calculated from the unabsorbed flux using the distances quoted in Table 1. Both flux and luminosity correspond to those of the best-fit model (power law or bremsstrahlung). It should be noted that since our selection criteria were based on a count rate cutoff, due to the variety of spectral forms, the inferred luminosity cutoff will not be uniform.

In Table 2 we denote the single-component model we choose as the better fit with an asterisk. This notation also indicates the model (power law or bremsstrahlung) used to compute the quoted flux. For $\approx 46\%$ of the power-law sources, the χ^2 difference (< 2) between the power-law and bremsstrahlung models is only marginally different. Of these sources, the average *kT* value for the bremsstrahlung fit is 5.54 keV. From our simulations we find that at high temperatures the bremsstrahlung fit becomes indistinguishable from a simple power law. Thus, given the high temperatures of the bremsstrahlung fits for these sources, they are equally well described by the power-law model. Typical *kT* bremsstrahlung values for accreting NSs are from 3.0 to 7.0 keV (Jones 1977).

3.1.1. Low-State ULXs

From these single-component sources, we classify 16 sources as low-state ULX sources. This classification is based on (1) the shape of the spectrum, well fitted by an absorbed power law, (2) the luminosity of the sources (they needed to be luminous enough to be included in our sample, $L_X > 10^{38}$ ergs s^{-1}), and (3) the X-ray location of the object within the optical galaxy (based on DSS images). The third criterion was important in limiting the effects of contamination from foreground and background sources within our sample of ULX sources. Thus, we overlaid X-ray contours from the *XMM-Newton* image on the DSS images, determining the location of the X-ray source as within or outside of the optical extent of the galaxy. We note that for two of the sources classified as low-state ULXs (Holmberg I XMM2 and NGC 2403 XMM4), there is uncertainty of whether the X-ray source is in fact within the optical galaxy due to the quality of the optical DSS images. The images used to determine the third criterion are available online.¹ We further discuss these criteria in § 4.

We state that the first criterion for classification as a low/hard-state ULX is a spectrum well fitted by a power law. Of the 30 sources in Table 2, 3 sources were clearly not well fitted by either the power-law or bremsstrahlung model. Seven of the

¹ See <http://www.astro.umd.edu/~lwinter/second3.html>.

TABLE 2
XMM-Newton BEST FIT: SINGLE-COMPONENT SPECTRAL FITS

| SOURCE | POWER LAW | | | BREMSSTRAHLUNG | | | F_X^c (10^{-12} ergs cm^{-2} s^{-1}) | L_X^d (10^{39} ergs s^{-1}) |
|----------------------------------|--|--|-----------------------|--|--|-----------------------|---|---|
| | n_{H}^a (10^{21} cm^{-2}) | Γ | χ^2/dof^b | n_{H}^a (10^{21} cm^{-2}) | kT (keV) | χ^2/dof^b | | |
| NGC 247 XMM2..... | 1.4 ^{+1.8} _{-1.1} | 2.29 ^{+1.02} _{-0.57} | 47.7/54* | <0.65 | 2.55 ^{+6.90} _{-1.61} | 48.8/54 | 0.33 | 0.38 |
| NGC 253 XMM2 (obs 1)..... | 1.6 ^{+0.4} _{-0.3} | 2.51 ^{+0.18} _{-0.17} | 69.1/74* | 0.5 ^{+0.2} _{-0.3} | 2.12 ^{+0.52} _{-0.37} | 74.7/74 | 0.52 | 0.87 |
| NGC 300 XMM4 ^c | 2.5 | 9.07 | 90.6/45 | | 0.27 | 0.14 | 117.6/45 | ... |
| NGC 1313 XMM4..... | 1.86 ^{+0.5} _{-0.4} | 1.8 ^{+0.07} _{-0.12} | 141.7/149* | 1.2 ^{+0.3} _{-0.3} | 6.62 ^{+2.3} _{-1.48} | 140.1/149 | 0.33 | 0.69 |
| IC 0342 XMM1..... | 5.8 ^{+0.6} _{-0.3} | 1.68 ^{+0.08} _{-0.08} | 159.5/185* | 4.9 ^{+0.5} _{-0.4} | 10.5 ^{+3.3} _{-1.9} | 160/185 | 3.5 | 6.37 |
| IC 0342 XMM2..... | 23.9 ^{+4.0} _{-3.6} | 1.85 ^{+0.22} _{-0.20} | 77.5/85* | 21 ^{+3.0} _{-2.8} | 8.5 ^{+0.0} _{-2.4} | 74.9/85 | 4.64 | 8.44 |
| IC 0342 XMM4..... | 5.3 ^{+1.4} _{-1.2} | 2.02 ^{+0.20} _{-0.19} | 64/58 | 4.2 ^{+0.99} _{-0.85} | 4.44 ^{+1.68} _{-0.74} | 56.9/58* | 0.69 | 1.26 |
| Mrk 71 XMM1..... | 0.47 ^{+0.30} _{-0.32} | 1.69 ^{+0.11} _{-0.13} | 55.3/54* | 0.04 ^{+0.26} _{-0.04} | 7.98 ^{+4.90} _{-2.92} | 59/56 | 0.19 | 0.27 |
| NGC 2403 XMM4..... | 1.7 ^{+0.8} _{-0.7} | 1.89 ^{+0.30} _{-0.25} | 62.3/71* | 1.1 ^{+0.5} _{-0.3} | 4.59 ^{+4.1} _{-1.5} | 62.3/71 | 0.31 | 0.48 |
| Holm II XMM1 (obs 2)..... | 1.5 ^{+0.2} _{-0.2} | 3.09 ^{+0.15} _{-0.12} | 266.7/252* | 0.31 ^{+0.12} _{-0.15} | 1.13 ^{+0.11} _{-0.11} | 309.4/252 | 3.5 | 3.1 |
| Holm I XMM2..... | 0.35 ^f | 2.13 ^{+0.16} _{-0.15} | 39.2/45* | 0.35 ^f | 2.07 ^{+0.57} _{-0.48} | 68.8/45 | 0.10 | 0.16 |
| Holm I XMM3..... | 0.35 ^f | 2.05 ^{+0.19} _{-0.18} | 34.4/32* | 0.35 ^f | 2.03 ^{+0.85} _{-0.56} | 42.1/32 | 0.12 | 0.19 |
| IC 2574 XMM1..... | 1.3 ^{+0.40} _{-0.30} | 1.97 ^{+0.07} _{-0.10} | 120.9/103 | 0.69 ^{+0.23} _{-0.25} | 4.1 ^{+0.89} _{-0.67} | 107.5/103* | 0.35 | 0.47 |
| IC 2574 XMM2..... | 0.4 ^{+0.4} _{-0.3} | 2.2 ^{+0.21} _{-0.09} | 45.7/51* | 0.229 ^g | 1.71 ^{+0.33} _{-0.27} | 65.4/52 | 0.22 | 0.34 |
| IC 2574 XMM3..... | 0.15 ^{+0.35} _{-0.14} | 2.43 ^{+0.27} _{-0.18} | 40.3/49* | 0.229 ^f | 0.97 ^{+0.18} _{-0.14} | 76.5/49 | 0.22 | 0.34 |
| NGC 4214 XMM1..... | 1.1 ^{+0.52} _{-0.47} | 1.87 ^{+0.26} _{-0.21} | 41.9/38* | 0.54 ^{+0.41} _{-0.35} | 4.86 ^{+4.52} _{-1.66} | 44.5/38 | 0.25 | 0.22 |
| NGC 4258 XMM2 (obs 2)..... | 6.7 ^{+2.6} _{-1.5} | 2.49 ^{+0.44} _{-0.33} | 83.6/57* | 4.8 ^{+1.3} _{-1.3} | 2.61 ^{+1.22} _{-0.92} | 85.5/57 | 0.30 | 1.9 |
| NGC 4258 XMM3..... | 1.4 ^{+0.69} _{-0.64} | 2.32 ^{+0.34} _{-0.24} | 38.9/37* | 0.49 ^{+0.44} _{-0.38} | 2.48 ^{+1.09} _{-0.74} | 41.3/37 | 0.20 | 1.2 |
| | 3.8 | 1.82 | 4/11* | 2.7 | 7.14 | 5/11 | 0.077 | 0.48 |
| NGC 4258 XMM4..... | 0.68 ^{+0.24} _{-0.42} | 1.97 ^{+0.22} _{-0.19} | 41.1/48* | 0.06 ^{+0.31} _{-0.05} | 4.07 ^{+1.6} _{-1.2} | 45.2/48 | 0.39 | 2.4 |
| | 1.9 ^{+0.78} _{-0.60} | 2.24 ^{+0.29} _{-0.24} | 77.03/77* | 0.9 ^{+0.6} _{-0.4} | 2.82 ^{+1.2} _{-0.8} | 77.8/77 | 0.33 | 2.0 |
| NGC 4395 XMM2..... | 0.33 ^{+0.6} _{-0.3} | 2.75 ^{+0.45} _{-0.39} | 38.6/36* | 0.133 ^f | 0.79 ^{+0.13} _{-0.13} | 52/37 | 0.15 | 0.28 |
| NGC 4395 XMM4..... | 0.3 ^{+0.6} _{-0.3} | 2.08 ^{+0.39} _{-0.30} | 16/25* | 0.133 ^f | 1.97 ^{+0.99} _{-0.60} | 21.6/26 | 0.15 | 0.28 |
| NGC 4449 XMM2..... | 1.5 ^{+0.3} _{-0.3} | 2.81 ^{+0.16} _{-0.14} | 103.5/112* | 0.25 ^{+0.2} _{-0.2} | 1.65 ^{+0.22} _{-0.21} | 112.1/112 | 0.29 | 0.33 |
| NGC 4490 XMM4..... | 10.2 ^{+2.3} _{-1.8} | 2.09 ^{+0.23} _{-0.19} | 51.6/50† | 8.3 ^{+1.3} _{-1.5} | 4.75 ^{+1.82} _{-0.90} | 50.3/50 | 0.84 | 6.1 |
| NGC 4490 XMM5..... | 3.9 ^{+0.94} _{-0.81} | 2.31 ^{+0.22} _{-0.20} | 60.1/65* | 2.5 ^{+0.54} _{-0.59} | 3.08 ^{+0.89} _{-0.62} | 61.6/65 | 0.41 | 2.98 |
| NGC 4631 XMM4 ^c | 7.8 | 9.50 | 261.5/74 | 2.9 | 0.17 | 207.8/74 | ... | ... |
| NGC 4631 XMM5 ^g | 1.3 | 1.03 | 641.8/153 | 1.3 | 199 | 659/153 | ... | ... |
| NGC 4945 XMM3..... | 3.3 ^{+1.3} _{-0.9} | 1.82 ^{+0.12} _{-0.20} | 30.1/30* | 2.5 ^{+0.83} _{-0.90} | 6.07 ^{+4.50} _{-1.71} | 30.3/30 | 0.38 | 0.43 |
| NGC 5204 XMM2..... | 0.89 ^{+0.49} _{-0.53} | 1.98 ^{+0.25} _{-0.20} | 42.37/42† | 0.23 ^{+0.3} _{-0.22} | 4.05 ^{+1.51} _{-0.95} | 42.2/42 | 0.15 | 0.41 |
| | 0.75 ^{+0.45} _{-0.45} | 1.63 ^{+0.20} _{-0.17} | 41.4/47* | 0.42 ^{+0.46} _{-0.38} | 7.82 ^{+5.05} _{-2.70} | 39.4/47 | 0.25 | 0.69 |
| M51 XMM3..... | 0.6 ^{+0.30} _{-0.40} | 1.86 ^{+0.09} _{-0.15} | 63.2/72* | 0.05 ^{+0.3} _{-0.02} | 5.22 ^{+2.26} _{-1.41} | 69.2/72 | 0.18 | 1.1 |
| M51 XMM4..... | 0.4 ^{+0.20} _{-0.30} | 1.55 ^{+0.08} _{-0.13} | 34.8/37* | 0.01 ^{+0.17} _{-0.13} | 11.1 ^{+0.32} _{-0.25} | 34.8/37 | 0.16 | 0.99 |

^a Total column density.

^b We denote with an asterisk the single-component model we choose as the better fit. Daggers represent the model we chose as the best fit while the difference in χ^2 between both models (power law and bremsstrahlung) is negligible.

^c Unabsorbed flux in the 0.3–10 keV band.

^d Unabsorbed luminosity in the 0.3–10 keV band, using the distances quoted in Table 1.

^e See Appendix B; supersoft X-ray source best fitted by single-component blackbody.

^f Absorption column density fixed to the galactic column density found in Table 1.

^g Source is best fitted by a combined power-law and vpec model; see Appendix B.

remaining 27 sources were clearly not within the optical extent of the host galaxy. Of the remaining sources excluded from classification as a low/hard-state object, IC 2574 XMM1 was better fitted with a bremsstrahlung model (with $\Delta\chi^2 = 13.4$). In an additional observation of the source NGC 4258 XMM2, a simple power-law model is not an adequate fit to the data (while the luminosity of the source is not within the ULX classification range mentioned in § 1). For the remaining sources, NGC 247 XMM2 and NGC 253 XMM2, there was sufficient doubt on the spectral form where the bremsstrahlung and power-law models, as well as the addition of a thermal component, all yielded adequate fits to the spectra. Therefore, we excluded these sources from a classification, noting the ambiguity of the model fits for these sources.

For those sources we classify as ULXs, we include computed bolometric luminosities in Table 3. To compute the bolometric luminosities for these ULX sources, we used the exponentially cutoff power-law spectrum of Magdziarz & Zdziarski (1995),

model `cutoffpl` in XSPEC, with a cutoff energy of 10 keV. From observational studies of Galactic X-ray binaries, it has been observed that low-state objects have spectra that cut off at high energies (≥ 10 –200 keV; Zdziarski & Gierliński 2004). Thus, we chose the exponential model `cutoffpl` over a simple power law. This also minimizes the total luminosity for flat power-law sources. We computed an unabsorbed bolometric flux in the 0.1–100 keV range through use of the `dummyresp` command (which extends the model beyond the observation's energy range). The luminosity was then computed using the distances listed in Table 1. We quote these values as L_{cutoffpl} (the luminosity obtained from extrapolating the power-law portion of the spectrum as an exponentially cutoff power law) in Table 3. We note that these values represent an upper limit on the bolometric luminosity for steep power-law ($\Gamma > 2$) objects, since we would expect the power-law component to cut off at some low energy. However, for shallow spectrum ($\Gamma < 2$) sources L_{cutoffpl} is a lower limit. This is because, schematically, a steep power law diverges

TABLE 3
BOLOMETRIC LUMINOSITIES OF ULX SOURCES

| Source | $L_{\text{cutoffpl}}^{\text{a}}$ (10^{39} ergs s^{-1}) | $L_{\text{bol}}^{\text{b}}$ (10^{39} ergs s^{-1}) | $M_{\text{Edd}}^{\text{c}}$ (M_{\odot}) | Class ^d |
|------------------------|--|---|--|--------------------|
| NGC 247 XMM1 | 13.4258 | 7.07734 | 54 | HS ULX |
| NGC 253 XMM1 | 9.31469 | 2.44574 | 19 | HS ULX |
| NGC 253 XMM2 | 4.3701 | 2.15292 | 17 | HS ULX |
| NGC 253 XMM6 | 5.05828 | 3.92514 | 30 | HS ULX |
| NGC 1313 XMM3 | 37.0364 | 27.9692 | 215 | HS ULX |
| NGC 1313 XMM4 | 1.50345 | ... | 116 | LS IMBH candidate |
| IC 0342 XMM1 | 14.1215 | ... | 1086 | LS ULX |
| IC 0342 XMM2 | 19.8129 | ... | 1524 | LS ULX |
| IC 0342 XMM3 | 114.015 | 95.4068 | 734 | HS ULX |
| Mrk 71 XMM1 | 0.2993 | ... | 23 | LS IMBH candidate |
| NGC 2403 XMM1 | 4.1497 | 2.14873 | 17 | HS ULX |
| NGC 2403 XMM4 | 0.57068 | ... | 44 | LS IMBH candidate |
| Holmberg II XMM1 | 0.88906 | ... | 68 | LS IMBH candidate |
| | 16.8335 | 11.4543 | 88 | HS ULX |
| Holmberg I XMM2 | 10.5158 | ... | 809 | LS ULX |
| M81 XMM1 | 15.7004 | 3.17932 | 24 | HS ULX |
| Holmberg IX XMM1 | 31.0582 | 28.1445 | 216 | HS ULX |
| NGC 4214 XMM1 | 0.26699 | ... | 21 | LS IMBH candidate |
| NGC 4258 XMM3 | 0.46503 | ... | 36 | LS IMBH candidate |
| NGC 4395 XMM1 | 9.04609 | 2.94683 | 23 | HS ULX |
| NGC 4449 XMM2 | 2.48586 | ... | 191 | LS IMBH candidate |
| NGC 4490 XMM1 | 16.8513 | 3.21972 | 25 | HS ULX |
| NGC 4490 XMM2 | 7.36612 | 4.51554 | 35 | HS ULX |
| NGC 4490 XMM3 | 240.653 | 176.04 | 1354 | HS ULX |
| NGC 4490 XMM4 | 1.66829 | ... | 128 | LS IMBH candidate |
| NGC 4490 XMM5 | 12.7136 | ... | 978 | LS ULX |
| NGC 4631 XMM1 | 10.6527 | 8.59661 | 66 | HS ULX |
| NGC 4736 XMM1 | 31.6561 | 27.3664 | 211 | HS ULX |
| NGC 4945 XMM3 | 0.44985 | ... | 35 | LS IMBH candidate |
| NGC 5204 XMM1 | 22.4756 | 2.20492 | 17 | HS ULX |
| NGC 5204 XMM2 | 5.57769 | ... | 429 | LS ULX |
| M51 XMM2 | 4.25898 | 3.57502 | 28 | HS ULX |
| M51 XMM3 | 2.10133 | ... | 162 | LS IMBH candidate |
| M51 XMM4 | 2.56064 | ... | 197 | LS IMBH candidate |
| M51 XMM6 | 46.7642 | 39.5189 | 304 | HS ULX |
| M101 XMM1 | 8.04916 | 7.68224 | 59 | HS ULX |
| M101 XMM2 | 7.54268 | 4.96709 | 38 | HS ULX |
| M101 XMM3 | 10.9792 | 1.03659 | 8 | HS ULX |
| NGC 5408 XMM1 | 20.9211 | 11.5369 | 89 | HS ULX |
| Circinus XMM1 | 70.3579 | 56.1033 | 432 | HS ULX |
| Circinus XMM2 | 208.746 | 0.69929 | 5 | HS ULX |
| Circinus XMM3 | 771.157 | 0.212957 | 2 | HS ULX |

^a Estimation of the bolometric luminosity, determined with an exponential cutoff in the power law at high energy (see text).

^b Bolometric luminosity estimate for high-state ULXs where the power law is cut at twice kT_{in} (see text).

^c Mass computed for objects radiating at $0.1L_{\text{Edd}}$ (low-state objects) or L_{Edd} (high-state objects; using L_{bol}).

^d Classification based on the criteria set forward in the text: high-state ULX (HS ULX), low-state ULX (LS ULX), and low-state IMBH candidate (low-state object with 10^{38} ergs $\text{s}^{-1} < L_{\text{bol}} < 3 \times 10^{39}$ ergs s^{-1}).

at low energies while a shallow power law diverges at high energies.

3.2. Two-Component Sources

For a number of sources, we found that an improvement in reduced χ^2 was achieved through fitting their spectra with an absorbed two-component blackbody and power-law model. We chose a simple blackbody model over the multicomponent disk model, `diskbb`, for purely schematic reasons. Namely, observations of galactic X-ray binary systems were fitted with blackbody models in the 1980s, when the S/N of these objects was comparable to that for our *XMM-Newton* data for ULX sources. We also note that the `diskbb` model does not give an entirely accurate

physical description of the data as it neglects the effects of general relativity. As a schematic model, the blackbody model is simpler than `diskbb`, with the same number of degrees of freedom. In addition, for low temperatures both models yield virtually identical temperatures. For this study, we chose the simpler model. We defer to a future paper a discussion of the different models for the thermal component.

In Table 4 we present the results for the sources that are fitted significantly better by the two-component model; these are sources where the improvement in χ^2 is greater than 8 (determined from our simulations in Appendix A). We include in Table 4 the improvement in χ^2 of the two-component fit over the simple power law. We include the power-law best fits to these sources

TABLE 4
XMM-Newton BEST FIT: TWO-COMPONENT BLACKBODY AND POWER-LAW SPECTRAL FITS

| Source | n_{H}^{a} (10^{21} cm^{-2}) | kT (keV) | Γ | χ^2/dof | $\Delta\chi^{2\text{b}}$ | F_{X}^{c} ($10^{-12} \text{ ergs cm}^{-2} \text{ s}^{-1}$) | L_{X}^{d} ($10^{39} \text{ ergs s}^{-1}$) |
|----------------------------|--|---|--|---------------------|--------------------------|---|--|
| NGC 247 XMM1 | 4.1 ^{+1.9} _{-1.5} | 0.12 ^{+0.03} _{-0.02} | 4.18 ^{+1.79} _{-2.52} | 86.5/93 | 25.7 | 6.2 | 7.1 |
| NGC 253 XMM1 | 2.7 ^{+0.4} _{-0.4} | 0.80 ^{+0.12} _{-0.09} | 1.74 ^{+0.17} _{-0.14} | 225.9/230 | 36.7 | 2.7 | 4.5 |
| | 7.3 ^{+1.1} _{-0.9} | 1.14 ^{+0.07} _{-0.10} | 2.54 ^{+0.27} _{-0.22} | 567/580 | 44.6 | 3.4 | 5.7 |
| NGC 253 XMM2 (obs 2)..... | 2.0 ^{+0.3} _{-0.2} | 0.71 ^{+0.10} _{-0.10} | 2.14 ^{+0.05} _{-0.08} | 460.3/498 | 47.1 | 1.6 | 2.7 |
| NGC 253 XMM3 | 3.1 ^{+4.8} _{-0.5} | 0.75 ^{+0.13} _{-0.10} | 2.47 ^{+2.99} _{-0.41} | 68.5/82 | 23.4 | 0.60 | 1.0 |
| | 3.2 ^{+0.7} _{-0.5} | 0.67 ^{+0.13} _{-0.09} | 2.07 ^{+0.20} _{-0.14} | 347.4/407 | 34.4 | 0.80 | 1.3 |
| NGC 253 XMM4 | 20 ^{+10.8} _{-7.6} | 0.11 ^{+0.03} _{-0.03} | 2.51 ^{+0.49} _{-0.30} | 66.7/57 | 6.9 | 15 | 25 |
| | 4.5 ^{+1.2} _{-1.9} | 0.09 ^{+0.02} _{-0.01} | 2.33 ^{+0.27} _{-0.22} | 309.3/291 | 12.1 | 1.4 | 2.2 |
| NGC 253 XMM5 | 1.5 ^{+7.2} _{-1.5} | 0.96 ^{+0.24} _{-0.32} | 2.43 ^{+3.06} _{-1.36} | 26.5/23 | 5.3 | 0.26 | 0.43 |
| | 4.6 ^{+1.1} _{-0.7} | 0.16 ^{+0.02} _{-0.03} | 1.95 ^{+0.14} _{-0.11} | 223.7/296 | 60.1 | 1.4 | 2.2 |
| NGC 253 XMM6 | 6.3 ^{+2.1} _{-1.1} | 0.12 ^{+0.02} _{-0.02} | 2.26 ^{+0.18} _{-0.12} | 417.9/407 | 17.1 | 1.9 | 3.1 |
| NGC 253 XMM7 | 6.3 ^{+0.9} _{-1.1} | 0.69 ^{+0.11} _{-0.12} | 2.40 ^{+0.41} _{-0.17} | 335.8/339 | 21.2 | 1.1 | 1.8 |
| NGC 300 XMM1 | 1.7 ^{+0.20} _{-0.30} | 0.98 ^{+0.14} _{-0.10} | 3.41 ^{+0.06} _{-0.26} | 443.7/420 | 26.1 | 1.3 | 1.0 |
| NGC 300 XMM2 | 3.8 ^{+1.7} _{-1.4} | 0.09 ^{+0.01} _{-0.01} | 2.87 ^{+0.34} _{-0.38} | 102.6/97 | 31.34 | 1.1 | 0.86 |
| NGC 300 XMM3 | 4.4 ^{+1.0} _{-0.8} | 0.04 ^{+0.25} _{-0.01} | 1.98 ^{+0.1} _{-0.1} | 87.7/79 | 14.2 | 1.2 | 0.93 |
| NGC 300 XMM6 | 2.3 ^{+2.6} _{-1.3} | 0.84 ^{+0.25} _{-0.19} | 4.9 ^{+1.97} _{-0.7} | 34.6/35 | 13 | 0.27 | 0.20 |
| NGC 1313 XMM1 | 3.0 ^{+1.2} _{-0.9} | 0.13 ^{+0.03} _{-0.02} | 1.75 ^{+0.14} _{-0.11} | 194.1/201 | 35.4 | 0.64 | 1.3 |
| NGC 1313 XMM2 | 3.1 ^{+0.4} _{-0.3} | 0.16 ^{+0.04} _{-0.02} | 2.27 ^{+0.10} _{-0.14} | 425.2/419 | 38.9 | 2.0 | 4.2 |
| NGC 1313 XMM3 | 6.2 ^{+0.8} _{-0.6} | 0.11 ^{+0.01} _{-0.01} | 2.76 ^{+0.10} _{-0.11} | 441.7/424 | 336.6 | 10 | 22 |
| IC 0342 XMM3..... | 9.7 ^{+1.8} _{-2.1} | 0.09 ^{+0.02} _{-0.01} | 2.69 ^{+0.16} _{-0.23} | 129.5/107 | 56.3 | 31 | 56.4 |
| NGC 1705 XMM1 | 0.29 ^{+0.39} _{-0.27} | 1.01 ^{+0.41} _{-0.29} | 2.31 ^{+0.89} _{-0.48} | 53/85 | 8.9 | 0.10 | 0.44 |
| NGC 1705 XMM3 | <1.44 | 1.07 ^{+0.20} _{-0.15} | 2.23 ^{+0.70} _{-0.56} | 69.8/65 | 11.1 | 0.15 | 0.48 |
| NGC 2403 XMM1 | 2.3 ^{+1.2} _{-1.1} | 0.66 ^{+0.16} _{-0.18} | 2.18 ^{+0.41} _{-0.59} | 81.4/79 | 10.8 | 1.99 | 3.1 |
| NGC 2403 XMM2 | 1.8 ^{+0.8} _{-0.6} | 0.62 ^{+0.16} _{-0.11} | 1.95 ^{+0.26} _{-0.42} | 163.1/151 | 16.4 | 1.0 | 1.6 |
| NGC 2403 XMM3 | 1.7 ^{+1.1} _{-0.8} | 0.74 ^{+0.23} _{-0.21} | 2.15 ^{+0.66} _{-0.40} | 84.2/105 | 8.4 | 0.64 | 1.1 |
| Holm II XMM1 (obs 1) | 1.6 ^{+0.1} _{-0.2} | 0.14 ^{+0.02} _{-0.01} | 2.35 ^{+0.05} _{-0.11} | 997.5/976 | 136.7 | 12 | 10 |
| M81 XMM1..... | 3.3 ^{+0.17} _{-0.08} | 0.90 ^{+0.03} _{-0.03} | 2.52 ^{+0.03} _{-0.04} | 1273.7/1243 | 533.1 | 4.5 | 7.0 |
| | 3.5 ^{+0.4} _{-0.6} | 1.13 ^{+0.13} _{-0.14} | 2.34 ^{+0.29} _{-0.36} | 203.5/204 | 21.4 | 4.8 | 7.4 |
| M81 XMM2..... | 7.4 ^{+0.5} _{-0.7} | 0.1 ^{+0.004} _{-0.004} | 2.87 ^{+0.16} _{-0.17} | 833.9/616 | 524.3 | 13 | 22 |
| M81 XMM4..... | 1.1 ^{+1.6} _{-1.0} | 2.51 ^{+1.11} _{-0.73} | 2.31 ^{+1.22} _{-1.05} | 48.9/50 | 28.2 | 0.43 | 0.70 |
| M81 XMM5..... | 0.15 ^{+0.69} _{-0.13} | 0.62 ^{+0.19} _{-0.11} | 1.26 ^{+0.22} _{-0.20} | 89/80 | 8.5 | 0.38 | 0.59 |
| Holm IX XMM1 | 2.1 ^{+0.2} _{-0.2} | 0.17 ^{+0.02} _{-0.02} | 1.72 ^{+0.04} _{-0.03} | 866.6/878 | 134.3 | 10 | 16 |
| NGC 4258 XMM1 | 0.38 ^{+0.96} _{-0.3} | 0.54 ^{+0.17} _{-0.08} | 1.51 ^{+0.4} _{-0.4} | 91.1/76 | 10.3 | 0.34 | 2.1 |
| NGC 4258 XMM2 (obs 1)..... | 1.9 ^{+2.4} _{-0.4} | 0.78 ^{+0.12} _{-0.13} | 2.02 ^{+0.65} _{-0.18} | 73.4/61 | 24.1 | 0.31 | 1.9 |
| NGC 4395 XMM1 | 2.0 ^{+0.08} _{-0.07} | 0.14 ^{+0.02} _{-0.02} | 3.44 ^{+0.34} _{-0.56} | 168.2/154 | 26.9 | 1.4 | 2.7 |
| NGC 4449 XMM1 | 8.7 ^{+4.8} _{-2.1} | 0.19 ^{+0.13} _{-0.07} | 2.21 ^{+0.33} _{-0.29} | 111.2/116 | 4.3 | 1.56 | 1.8 |
| NGC 4449 XMM3 | 3.5 ^{+1.3} _{-0.9} | 0.15 ^{+0.03} _{-0.03} | 2.52 ^{+0.36} _{-0.39} | 119.9/87 | 34.1 | 1.1 | 1.3 |
| NGC 4490 XMM1 | 5.8 ^{+2.96} _{-2.96} | 0.77 ^{+0.08} _{-0.095} | 2.89 ^{+1.77} _{-0.61} | 66.5/63 | 35 | 0.88 | 6.4 |
| NGC 4631 XMM1 | 3 ^{+0.9} _{-0.5} | 0.12 ^{+0.03} _{-0.02} | 2.12 ^{+0.03} _{-0.02} | 371.3/345 | 12.1 | 0.96 | 6.5 |
| NGC 4631 XMM2 | 2.3 ^{+1.4} _{-0.3} | 0.18 ^{+0.05} _{-0.06} | 1.80 ^{+0.12} _{-0.09} | 107.4/97 | 12.1 | 0.25 | 1.7 |
| NGC 4631 XMM3 | 1.1 ^{+1.1} _{-0.8} | 1.01 ^{+0.12} _{-0.1} | 2.45 ⁺¹ _{-0.62} | 127.1/96 | 18.9 | 0.15 | 1.0 |
| NGC 4945 XMM1 | 3.5 ^{+2.1} _{-1.1} | 0.77 ^{+0.27} _{-0.10} | 1.60 ^{+0.40} _{-0.31} | 96.1/120 | 20 | 0.59 | 0.68 |
| NGC 4945 XMM2 | 3.2 ^{+1.1} _{-0.7} | 1.15 ^{+0.28} _{-0.33} | 1.80 ^{+0.20} _{-0.30} | 105.8/113 | 8.7 | 0.66 | 0.76 |
| NGC 4945 XMM4 | 4.0 ^{+2.0} _{-1.1} | 0.61 ^{+0.10} _{-0.10} | 2.82 ^{+1.06} _{-0.58} | 58.4/60 | 17.1 | 0.38 | 0.44 |
| NGC 5204 XMM1 | 0.66 ^{+0.35} _{-0.08} | 0.16 ^{+0.02} _{-0.03} | 1.92 ^{+0.12} _{-0.06} | 543.0/559 | 49.1 | 1.98 | 5.6 |
| | 1.1 ^{+0.08} _{-0.14} | 0.16 ^{+0.02} _{-0.02} | 2.03 ^{+0.12} _{-0.12} | 461.4/496 | 71.6 | 2.92 | 8.0 |
| M51 XMM1..... | 0.95 ^{+1.10} _{-0.18} | 0.16 ^{+0.03} _{-0.05} | 2.15 ^{+0.42} _{-0.17} | 97/80 | 13.4 | 0.31 | 1.9 |
| M51 XMM5..... | 10.4 ^{+1.7} _{-3.7} | 0.078 ^{+0.01} _{-0.01} | 2.26 ^{+0.26} _{-0.25} | 59.8/70 | 196.2 | 220 | 1900 |
| M83 XMM4..... | 1.77 ^{+0.9} _{-1.77} | 0.54 ^{+0.18} _{-0.09} | 1.61 ^{+0.36} _{-0.31} | 84.8/89 | 6.6 | 0.2 | 0.92 |
| M101 XMM1..... | 0.22 ^{+0.12} _{-0.15} | 0.21 ^{+0.03} _{-0.04} | 1.42 ^{+0.14} _{-0.05} | 249.9/231 | 53.1 | 0.45 | 2.9 |
| M101 XMM2..... | 1.6 ^{+0.46} _{-0.21} | 0.76 ^{+0.14} _{-0.10} | 1.88 ^{+0.25} _{-0.11} | 251.6/261 | 37.2 | 0.7 | 4.6 |
| NGC 5408 XMM1 | 0.9 ^{+0.21} _{-0.16} | 0.14 ^{+0.01} _{-0.01} | 2.71 ^{+0.16} _{-0.20} | 316.4/337 | 80.4 | 3.97 | 10.9 |
| Circinus XMM1..... | 10.1 ^{+1.2} _{-1.2} | 0.10 ^{+0.01} _{-0.01} | 2.30 ^{+0.08} _{-0.08} | 749.4/861 | 13.5 | 12 | 23 |
| Circinus XMM2..... | 11.2 ^{+2.4} _{-1.7} | 0.53 ^{+0.03} _{-0.03} | 4.71 ^{+0.94} _{-0.49} | 438.5/430 | 79.4 | 5.6 | 10.7 |
| Circinus XMM3..... | 13.5 ^{+5.5} _{-5.6} | 0.67 ^{+0.10} _{-0.08} | 5.77 ^{+2.24} _{-2.3} | 269.3/260 | 15.9 | 7.6 | 14.5 |

^a Total column density.

^b Improvement in χ^2 over the single-component power-law model.

^c Unabsorbed flux in the 0.3–10 keV band.

^d Unabsorbed luminosity in the 0.3–10 keV band, using the distances quoted in Table 1.

TABLE 5
XMM-Newton Two-Component Blackbody and Power-Law Spectral Fits for Sources with Large Uncertainty

| Source | n_{H}^{a} (10^{21} cm^{-2}) | kT (keV) | Γ | χ^2/dof | $\Delta\chi^{2\text{b}}$ | F_{X}^{c} ($10^{-12} \text{ ergs cm}^{-2} \text{ s}^{-1}$) | L_{X}^{d} ($10^{39} \text{ ergs s}^{-1}$) |
|----------------------|--|------------------------|------------------------|---------------------|--------------------------|---|--|
| NGC 300 XMM5 | $0.41^{+0.60}_{-0.30}$ | $1.06^{+0.37}_{-0.20}$ | $2.78^{+0.61}_{-0.65}$ | 46.6/53 | 7.6 | 0.17 | 0.13 |
| NGC 1705 XMM2 | $0.96^{+0.97}_{-0.32}$ | $0.23^{+0.10}_{-0.11}$ | $1.60^{+1.97}_{-0.27}$ | 85.5/74 | 6.5 | 0.09 | 0.27 |
| Holm I XMM1 | $0.4^{+0.5}_{-0.3}$ | $1.97^{+0.66}_{-0.89}$ | $2.46^{+0.44}_{-0.40}$ | 97.4/93 | 5.4 | 0.6 | 0.93 |
| M81 XMM3 | $3.7^{+2.4}_{-2.1}$ | $0.11^{+0.05}_{-0.02}$ | $1.69^{+0.27}_{-0.33}$ | 77.1/78 | 4.25 | 0.53 | 0.82 |
| Sextans A XMM1 | $0.4^{+0.7}_{-0.1}$ | $1.05^{+2.3}_{-0.07}$ | $2.6^{+0.8}_{-0.2}$ | 269.1/271 | 2.3 | 0.60 | 0.14 |
| NGC 4214 XMM2 | $1.8^{+1.9}_{-0.6}$ | $0.81^{+0.56}_{-0.21}$ | $3.95^{+1.81}_{-1.05}$ | 46.4/44 | 4.5 | 0.4 | 0.35 |
| NGC 4395 XMM3 | $0.5^{+0.9}_{-0.3}$ | $1.10^{+0.67}_{-0.18}$ | $2.66^{+1.05}_{-0.77}$ | 52/56 | 3.9 | 0.29 | 0.56 |
| NGC 4490 XMM2 | $4.4^{+1.9}_{-1.9}$ | $0.60^{+0.20}_{-0.12}$ | $2.13^{+0.50}_{-0.70}$ | 42.4/54 | 7.1 | 0.65 | 4.7 |
| NGC 4490 XMM3 | $13^{+9.6}_{-2.5}$ | $0.09^{+0.02}_{-0.02}$ | $3.21^{+0.52}_{-0.17}$ | 72.1/78 | 4.6 | 12 | 87.4 |
| NGC 4736 XMM1 | $6.3^{+3.0}_{-3.7}$ | $0.08^{+0.03}_{-0.02}$ | $2.41^{+0.34}_{-0.27}$ | 54.9/51 | 7.9 | 8.1 | 17.9 |
| M51 XMM2 | $1.3^{+0.6}_{-0.5}$ | $0.26^{+0.07}_{-0.08}$ | $1.80^{+0.61}_{-0.92}$ | 70.7/68 | 4.5 | 0.36 | 3.0 |
| M51 XMM6 | $8.2^{+3.5}_{-5.6}$ | $0.08^{+0.05}_{-0.02}$ | $3.0^{+0.37}_{-0.43}$ | 36.9/41 | 4.07 | 5.6 | 35 |
| M51 XMM7 | $2.8^{+3.4}_{-2.1}$ | $0.10^{+0.03}_{-0.03}$ | $1.97^{+0.43}_{-0.30}$ | 31.7/29 | 6.1 | 0.26 | 1.6 |
| M83 XMM1 | $1.6^{+0.48}_{-0.45}$ | $0.74^{+0.23}_{-0.26}$ | $2.58^{+0.60}_{-0.24}$ | 177.7/209 | 4.7 | 0.63 | 2.5 |
| M101 XMM3 | $1.98^{+1.0}_{-0.61}$ | $0.63^{+0.22}_{-0.20}$ | $2.93^{+0.15}_{-0.26}$ | 145.5/131 | 3.4 | 0.56 | 3.7 |
| M101 XMM4 | $1.8^{+0.17}_{-0.15}$ | $0.54^{+0.11}_{-0.07}$ | $2.22^{+0.12}_{-0.08}$ | 158.2/138 | 7.5 | 0.34 | 2.2 |
| M101 XMM5 | $1.3^{+1.2}_{-0.2}$ | $0.18^{+0.05}_{-0.06}$ | $1.95^{+0.3}_{-0.22}$ | 45.1/44 | 2.8 | 0.13 | 0.85 |

^a Total column density.

^b Improvement in χ^2 over the single-component power-law model.

^c Unabsorbed flux in the 0.3–10 keV band.

^d Unabsorbed luminosity in the 0.3–10 keV band, using the distances quoted in Table 1.

in Appendix C for comparison with other analyses. In order to determine whether the blackbody component is statistically significant for the sources fitted with a two-component model, we simulated spectra based on accurate modeling of some of the brightest sources: NGC 247 XMM1, NGC 5408 XMM1, and Holmberg II XMM1. These sources span the observed range of the ratios of the blackbody to power-law component and thus represent those from our sample with a weak blackbody relative to the power-law component, intermediate case, and a strong blackbody, respectively. Our simulations are described in full in Appendix A. We found that, using a $\Delta\chi^2 > 8$ criterion, which corresponds to the 99% significance level as according to the F -test for the addition of two extra parameters, we can readily detect the strong and intermediate thermal components in all spectra with more than 400 counts. The weak thermal emission cannot be detected in 400 count spectra but is readily detected in 2000 count spectra. This gives us confidence that our results are statistically meaningful.

3.2.1. High-State ULXs

Of the sources in Table 4, we classified high-state (or thermal dominated) ULX sources based on three criteria: (1) spectra characterized by an absorbed power-law and blackbody model, (2) luminosity, and (3) X-ray source within the optical extent of the host galaxy. The luminosity criteria required that these sources have unabsorbed luminosities $L_{\text{X}} \gtrsim 3 \times 10^{39} \text{ ergs s}^{-1}$ (we used $L_{\text{X}} = 2.7 \times 10^{39} \text{ ergs s}^{-1}$ as our hard cutoff). If the sources are radiating at the Eddington luminosity, this cutoff luminosity corresponds to objects with masses greater than $20 M_{\odot}$.

From Table 4, 27 observations are recorded with $L_{\text{X}} > 2.7 \times 10^{39} \text{ ergs s}^{-1}$. The addition of a thermal component to these sources is statistically significant over a pure power-law model. Of the 27 observations, 3 correspond to multiple observations of a single source. From an analysis of the DSS images, all 24 of these sources are within the optical extent of their host galaxies. However, M51 XMM5 appears to be coincident with the center of its host, a dwarf companion galaxy to M51. The location, coupled with the high luminosity ($L_{\text{X}} = 1.9 \times 10^{42} \text{ ergs s}^{-1}$), leads

us to classify this source as an AGN. We also excluded two sources (NGC 1313 XMM2 and M81 XMM2) from our sample of high/soft-state ULXs due to their previous identification as supernovae. Of the remaining 21 sources, NGC 253 XMM4 had a luminosity of $2.5 \times 10^{40} \text{ ergs s}^{-1}$ in one observation and $2.2 \times 10^{39} \text{ ergs s}^{-1}$ in a second. This significant change in luminosity, with one observation below our luminosity cutoff and another a factor of ≈ 10 higher than the other, led us to exclude this source as a high/soft-state ULX. It is likely that this source is a stellar mass X-ray binary within its host galaxy, where one of the observations captured the source in an outburst.

In Table 5 we list sources that have $\Delta\chi^2$ values less than 8 for a single observation. Most of these sources have weak blackbody normalizations compared to the power-law normalization. We classify these sources as being well fitted by a two-component model while acknowledging the uncertainty in the fit as determined by the simulations. The addition of the thermal component is not significant enough for these sources to be classified with certainty in either Table 2 or Table 4. The simple power-law fits for these sources are included with those for sources in Table 8. We note that due to their high luminosity, we included six of these sources (NGC 4490 XMM2, NGC 4490 XMM3, NGC 4736 XMM1, M51 XMM2, M51 XMM6, and M101 XMM3) with uncertain fit parameters as ULX high-state sources. Two of these sources (NGC 4490 XMM3 and M51 XMM6) had unabsorbed luminosities > 10 times the $3 \times 10^{39} \text{ ergs s}^{-1}$ cutoff used for high-state ULX classification. The other four sources had luminosities above the threshold, as well as weak blackbody components compared to the power law (see Appendix A for simulations). We used these points to justify including these sources with the Table 4 sources in the following discussions with the proviso that their spectral fits do not indicate absolutely the necessity of the additional thermal component. For this reason, we denote these sources with a special symbol (a circle) in subsequent figures while including them as high-state ULX objects.

For our ULX sources modeled by a combined blackbody and exponentially cutoff power law, we computed bolometric luminosities using two methods. The first method is recorded as L_{cutoffpl} in

Table 3. We computed the flux in the range 0.1–100 keV using an unabsorbed blackbody and exponentially cutoff power-law model using the XSPEC command `dummyresp`. For the second method, recorded as L_{bol} in Table 3, we estimate a more accurate bolometric luminosity calculated from the flux in the range of $2kT$ –100 keV, where kT is the blackbody temperature obtained from the model. In Galactic X-ray binary systems, the power-law component of the X-ray spectrum is believed to be from Comptonization in a corona. The photons supplying this energy originate from the blackbody continuum emanating from the accretion disk. Thus, a natural cutoff for this power-law component occurs at the peak emission of the blackbody (which is approximately $3kT$). The estimated values (obtained from cutting off the combined unabsorbed blackbody and cutoff power-law model at the value $2kT$) differ with regard to the full estimate (flux from the fully integrated blackbody added to the separate flux from the cutoff power law from $3kT$ to 100 keV) depending on the normalization factors used (for both the blackbody temperature and the spectral index Γ). Choosing three sources displaying a range of blackbody to power-law strength (Holmberg II XMM1, NGC 253 XMM1, and IC 0342 XMM3), we found that the estimated values were within 88.3%, 95.1%, and 96.8%, respectively, of the more complete estimation. Given their close proximity (within approximately 90%), we quote these estimated values as a good approximation to the bolometric luminosity.

We note that our bolometric luminosities for all of the classified ULX sources, on average, are a factor of 1.08 greater than the X-ray luminosities in the 0.3–10 keV band for the objects best fitted by a combined blackbody and power law. Thus, to good approximation, the X-ray luminosity is the bolometric luminosity. However, for the objects best fitted by a simple power law (low-state ULX sources), the average bolometric luminosity is roughly a factor of 7 greater than the X-ray luminosity in our band. This average is dominated by the steep power-law objects, in particular Holmberg II XMM1 ($\Gamma = 3.09$). Excluding this object, we get an average bolometric luminosity that is 2.8 times the X-ray flux and more indicative of the general properties of these power-law-fitted objects.

3.3. Additional Sources

In addition, in this large sample of point sources, we came across a number of objects whose spectra were not well fitted by the models we employed. These sources have luminosities exceeding $L_X \approx 10^{38}$ ergs s^{-1} , if they are associated with the host galaxy, and are placed in Tables 2 and 4, as well as Appendix B. These sources include two supersoft sources, one possible AGN, and three sources well fitted with additional absorption models (including a partial covering model and a model of hot gas). We briefly describe these sources in Appendix B.

4. DISCUSSION

We have determined best-fit spectral parameters of the bright X-ray sources in 32 nearby galaxies. In choosing three “standard” models for our study, we hoped to accurately separate high- and low-state ULXs from other types of luminous X-ray sources. We specifically chose to fit the data with the bremsstrahlung model in order to identify NS X-ray binaries within our sample. The models we used are purely schematic, and they do not physically explain the phenomena occurring, but they are standard and qualitatively simple models often used to fit the spectra of Galactic X-ray binaries.

We cross-referenced the X-ray positions of our sources with both NED and SIMBAD in order to identify known supernovae, galaxies, and stars. In addition, we examined the DSS optical

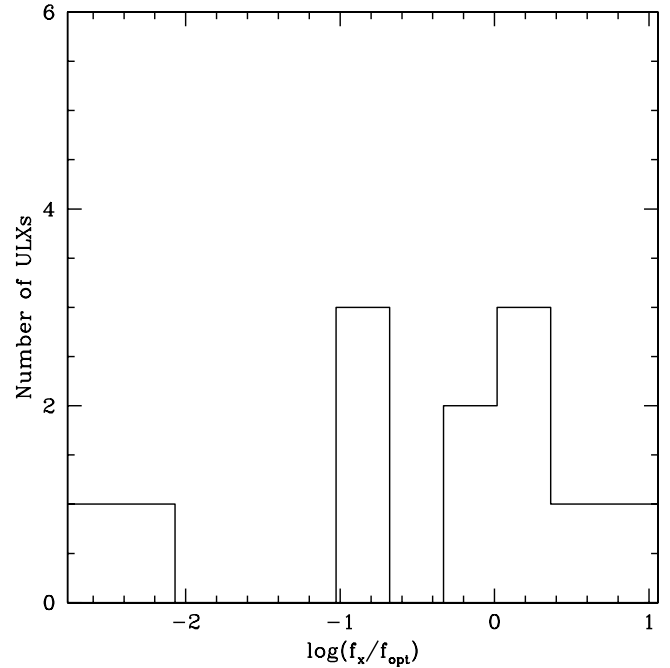


FIG. 2.— Distribution of f_x/f_{opt} for the brightest possible optical point source within the *XMM-Newton* error circle. We define f_x as the unabsorbed X-ray flux in the 0.3–10 keV range and f_{opt} as the optical flux obtained from the *U* filter of *XMM-Newton*’s OM (as described in text). These ratios do not represent the actual f_x/f_{opt} of the sources but are an estimate of the minimum possible value. A majority of the sources had no optical point source within the X-ray contour and thus have ratios of f_x/f_{opt} far higher than those indicated in the plot.

images to place the position of our sources within their respective galaxies. Such analysis aimed to minimize contamination of our sample of ULXs with bright background and foreground sources.

Further, we examined *XMM-Newton*’s Optical Monitor (OM) data in the visual bands (*U*, *B*, *V*). The *XMM-Newton* PPS contain point-source detection files for the OM data. We overlaid these point-source detections with X-ray contour maps in order to determine the brightest possible optical count rates for the X-ray sources, which were then converted into fluxes using the OM calibration documentation. In Figure 2 we plot the distribution of the logarithm of the X-ray to optical flux for the brightest possible optical counterpart inside the *XMM-Newton* error circle. Only 13 of the 32 host galaxies had visible band OM data during the observations. Of these 13 galaxies, 40 of the X-ray sources were in the range of the OM data and only 14 were coincident with an optical point source. Therefore, the majority of our sources have X-ray/optical flux ratios that are larger than those displayed. Figure 2 illustrates the lowest possible X-ray/optical flux ratios and also, by the sparsity of sources included in the diagram, illustrates the fact that a majority of the sources have no obvious optical counterpart and thus have very large X-ray/optical flux ratios. We estimate the point-source detection limit of the OM *U* filter as approximately 1.24×10^{-14} ergs $\text{cm}^{-2} \text{s}^{-1}$. For an unabsorbed X-ray flux of 1.0×10^{-12} ergs $\text{cm}^{-2} \text{s}^{-1}$, typical of objects with $L_X \approx 2 \times 10^{38}$ ergs s^{-1} located at a distance of 8 Mpc, this corresponds to $\log(f_x/f_{\text{opt}}) = 1.9$. Therefore, the average value for our sources should fall around 2 or greater. The average distribution for QSOs and AGNs centers around 0 and 0.8 for BL Lac objects (Anderson et al. 2003). Our objects have ratios of L_X/L_{opt} at least 10 times higher than those of AGNs and 100 times greater than stars.

Recently, Gutiérrez & López-Corredoira (2005) identified six ULXs from the catalog of Colbert & Ptak (2002) as QSOs. They

hypothesized that a large number of ULXs may in fact be quasars at higher redshift than their supposed host galaxy. However, unlike the objects studied in Gutiérrez & López-Corredoira (2005), our ULX sources are all spatially coincident with the optical host galaxy. In addition, a majority of our ULXs are not in the proximity of a noticeable optical point source. The X-ray/optical flux ratios of our sources are much larger, on average, than might be expected for a QSO. It is also worth noting that while some cataloged ULXs may be QSOs, optical identifications have been made associating other ULXs with a type B supergiant companion (Kuntz et al. 2005; Liu et al. 2004).

4.1. Classification Criteria

The spectral fits indicate that to high statistical probability (see Appendix A) we can distinguish a class of low-state ULXs from the high-state objects. This is assuming, as indicated in § 1, that ULXs are isotropic emitters with luminosity and spectral form similar to Galactic stellar mass X-ray binaries. In § 3 we stated that our ULX classification depends on three criteria: (1) spectral form, (2) luminosity, and (3) location of the X-ray source within the optical host galaxy (as determined from the DSS images). We have chosen simple, parametric “nonphysical” models for the spectra because the S/N of most of the observations does not allow anything else to be constrained.

Of the sources in Table 2, 16 are classified as low-state objects or low/hard-state ULXs, having unabsorbed luminosities $>10^{38}$ ergs s^{-1} and spectra that are well fitted by power-law models. Throughout this paper we use the term low-state ULXs to include “low-state IMBH candidates” (sources with $L_X \lesssim 3 \times 10^{39}$ ergs s^{-1} and spectra well fitted by a simple absorbed power law) and low-state sources with luminosities that clearly classify them as ULX sources ($L_X \gtrsim 3 \times 10^{39}$ ergs s^{-1}). These low-state ULX sources are listed in Table 3.

In § 3 we noted that a power-law model and high-temperature bremsstrahlung model are indistinguishable. Therefore, it is important to consider the luminosity of these sources in the claim that they are not NS X-ray binaries accreting at the Eddington luminosity. Of the low-state ULX sources, only 2 of the 16 sources have bolometric luminosities below the Eddington luminosity of a $3 M_\odot$ object ($\approx 4 \times 10^{38}$ ergs s^{-1}), corresponding to the maximum mass of an NS. All of the sources have values exceeding the Eddington limit for a $2 M_\odot$ NS.

Further, 26 sources have unabsorbed $L_X \gtrsim 3 \times 10^{39}$ ergs s^{-1} , corresponding to $L \approx L_{\text{Edd}}$ at $M > 20 M_\odot$ as expected for high-state IMBHs, and spectra that are well fitted by combined blackbody and power-law models. These are high-state objects. The spectral fits for these sources are listed in Tables 4 and 5. In a statistical sense, we find that the greater the number of counts in the observation, the greater our confidence in the thermal component contributing to a better fitting model. We explain our confidence levels obtained from spectral simulations in Appendix A.

In addition to these high- and low-state ULXs, we find a large number of sources best fitted by a combined blackbody and power-law model but below our threshold of $L_X \approx 3 \times 10^{39}$ ergs s^{-1} for a high-state ULX (listed in Table 4). Many of these sources may be accreting stellar mass BHs with $M < 20 M_\odot$. Some of these non-ULX sources were found away from the optical extent of the targeted galaxy (from our analysis of the DSS images) and therefore may be background AGNs.

4.2. Low-State ULXs

For Galactic BH X-ray binaries, spectral indices of low-state (or power law dominated) objects are typically lower than those of

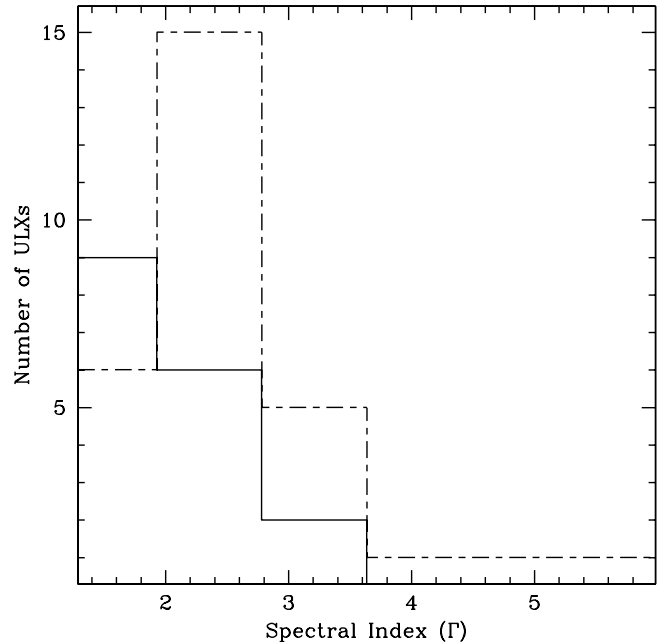


FIG. 3.—Distribution of the spectral indices (Γ) for low-state (solid line) and high-state (dashed line) objects. For Galactic low-state objects, typically $\Gamma \approx 2.0$, similar to our sample, while the high-state objects have a steeper Γ (Remillard & McClintock 2006).

high-state objects, with $\langle \Gamma \rangle_{\text{low}} \approx 1.7$ and $\langle \Gamma \rangle_{\text{high}} \approx 2.5$ (Remillard & McClintock 2006). In Figure 3 we plot the distribution of the spectral index for both high- and low-state objects. The spectral index for the high-state objects is the value of Γ from the two-component fit. As in the Galactic sources, it is clear that the spectral indices of the high-state objects are indeed larger. Of further interest, the distribution of spectral index for low-state objects looks remarkably similar to the distribution of spectral index for moderate-luminosity quasars, many of which are thought to be the analogs of low-state BHs (Porquet et al. 2004). This supports the classification of these objects as accreting BHs.

For the high-state objects, we find mean values of $\Gamma = 2.46$, with an rms deviation of $S = 0.12$, and $L_X = 1.4 \times 10^{40}$ ergs s^{-1} , $\log S = 1.6$. This calculation excludes the three objects with spectral indices greater than 3.5. For the low-state objects, we find mean values of $\Gamma = 2.09$, with an rms deviation of $S = 0.10$, and $L_X = 2.2 \times 10^{39}$ ergs s^{-1} , $\log S = 2.1$. This value of $\Gamma = 2.1$ is softer than the typical hard-state value of ≈ 1.7 but within the $1.5 < \Gamma < 2.1$ range used to classify this state for Galactic X-ray binaries (Remillard & McClintock 2006). Computing a Kolmogorov-Smirnov two-sample test, separating the sources into the category of low state or high state, we find a likelihood of approximately 0.03 that the spectral indices belong to the same distribution.

The low/hard X-ray state of X-ray binaries is associated with a low accretion rate from the companion object with $L \lesssim 0.1 L_{\text{Edd}}$ (Done & Gierlinski 2003). Therefore, on average, we expect the luminosities of the low-state objects to be lower than the high-state objects. Figure 4 displays the luminosity of the objects as a function of the spectral index. On average, the highest luminosity low-state objects have luminosities lower than those of the high-state objects.

The lower L_X values of the low-state objects imply that they may indeed be accreting at a lower rate than the high-state objects. This can further be seen in the bolometric luminosities listed in Table 3. If these objects are accreting at a rate similar to

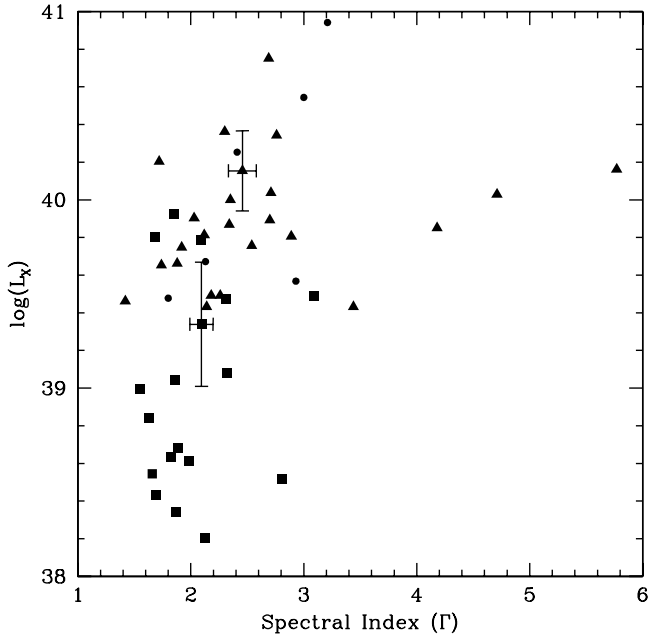
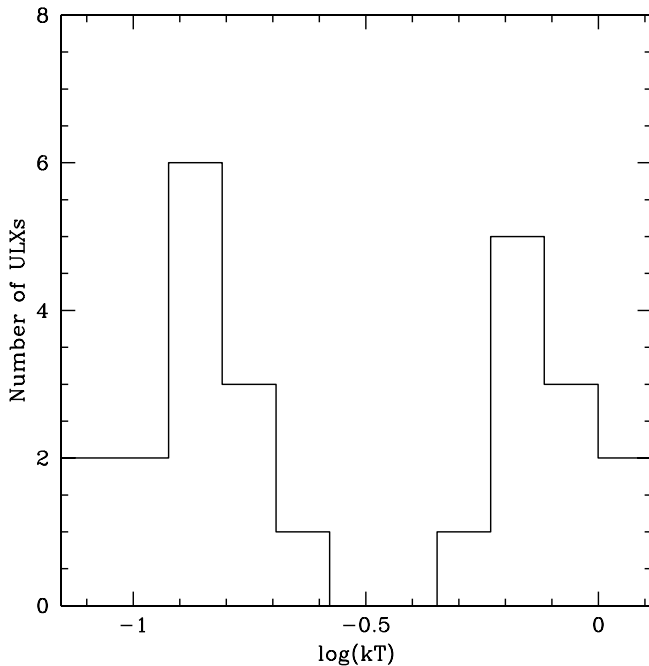


FIG. 4.—Relationship of luminosity vs. spectral index for low-state (*rectangles*) and high-state (*triangles*) objects. Sources represented by a circle are those where the $\Delta\chi^2$ value between the two-component and power-law fits was very small. As expected from observations of Galactic stellar mass BH systems (Remillard & McClintock 2006), the classified low-state ULXs in our sample have, on average, lower X-ray luminosities than the corresponding high-state ULXs. We plot the mean values for both high-state and low-state objects with error bars indicating the rms deviation. The outlying objects with spectral indices greater than 3.5 were not included in the mean or deviation calculations.

Galactic low/hard-state BHs ($0.1L_{\text{Edd}}$; Done & Gierlinski 2003), we can estimate their masses as

$$\frac{M}{M_{\odot}} = \frac{L_{\text{bol}}}{0.1L_{\text{Edd}}},$$



with L_{Edd} as the Eddington luminosity for a $1 M_{\odot}$ object (1.3×10^{38} ergs s^{-1}). Our mass estimations, based on our limits to the bolometric luminosities, yield masses of 20–1500 M_{\odot} (see Table 3), precisely what we might expect for a population of IMBHs.

4.3. High-State ULXs

If the high-state (thermal dominated) ULXs represent a class of IMBH systems, their X-ray spectra should be well described by a combined blackbody and power-law model. Scaling for the mass of the BH, we would expect a relationship of $T \propto M^{-1/4}$ between BH mass and blackbody temperature (Makishima et al. 2000). This would indicate a thermal component of ~ 100 eV for masses of $\sim 10^3 M_{\odot}$. A few objects have been reported to display this property (Miller et al. 2003; Roberts et al. 2005). In Figure 5 we graph the distribution of the thermal component for our classified high-state objects.

We find that there are two peaks in the distribution among the thermal component, one at approximately 100 eV and another centered close to 1 keV. This could indicate two different classes among the high-state objects. It is possible that those objects with blackbody components near 100 eV are indeed high-state IMBHs. We note that the soft excess in PG quasars has also been modeled as a blackbody with $kT_{\text{soft}} \approx 100$ eV, but it has been suggested that this could be the result of a process not directly related to BH accretion (such as the presence of a warm absorber; Gierliński & Done 2004). Another possible explanation is that the soft component is the result of ionized reflection from the disk (Ross & Fabian 2005). While the possibility exists that the “thermal” component of these 100 eV sources is not directly related to BH accretion or is related in a “nonthermal” (i.e., ionized reflection) sense, as may be the case with the soft excess in PG quasars, we assume that the soft component for the objects we classify as high-state ULXs originates from a thermal disk. We use this assumption to test the IMBH hypothesis; thus, speculation on the nature of the soft component is beyond the scope of this paper.

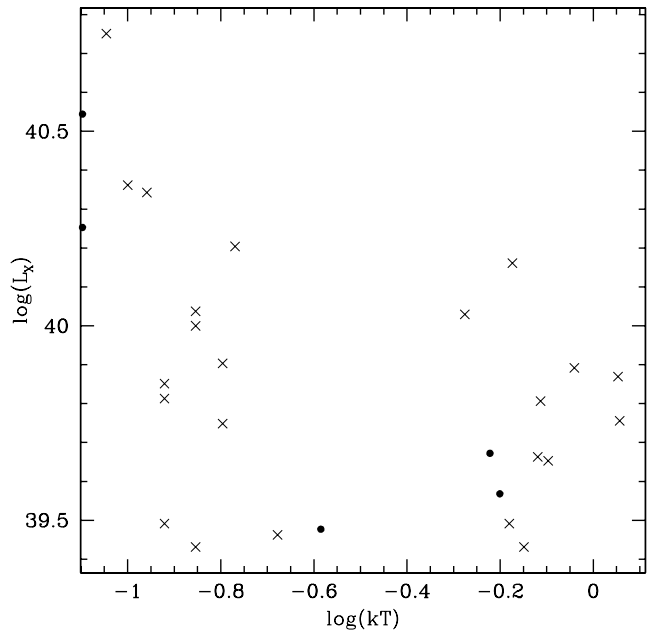


FIG. 5.—*Left*: Distribution of the blackbody temperature for high-state objects. *Right*: Relationship of blackbody temperature vs. luminosity (in the 0.3–10 keV band) for high-state objects. We see two peaks arise in the distribution, one centered around $kT \approx 0.1$ and another at $kT \approx 1$. The peak with a low disk temperature also corresponds to the highest luminosities, suggesting that these may be high-state IMBHs. The sources with higher disk temperature also have lower luminosities. The spectra of these sources were also well fitted by an inverse Comptonization model (a model successfully used to fit some of the Galactic BH X-ray binaries in the very high state).

The second peak, centered around 1 keV, has a temperature reminiscent of the Galactic BH systems in our own Galaxy. These systems may thus be stellar mass BHs accreting matter near the Eddington limit. If this were the case, we would expect the luminosities of the sources exhibiting a higher blackbody temperature to be lower than those with cooler blackbody components. In the right panel of Figure 5, we plot the relationship between blackbody temperature and L_X in the 0.3–10 keV band. Once again, two groups are seen in the distribution of high-state ULXs. The most luminous objects are those with low blackbody temperatures. On average, the less luminous sources exhibit higher blackbody temperatures. For the sources with $L_X > 10^{40}$ ergs s^{-1} , the mean blackbody temperature is 0.31, while the sources below this luminosity threshold have a mean blackbody temperature of 0.61.

The second, low-luminosity group in the distribution of high-state ULXs is clearly distinguishable in both panels of Figure 5. We found that, with the exceptions of NGC 253 XMM1, M81 XMM1, and NGC 5204 XMM1, the spectra of these objects could also be well described by an absorbed Comptonization (compST) model (Sunyaev & Titarchuk 1980) used to fit galactic BHs in the very high state when they are radiating at the Eddington limit. This model simulates Compton scattering of cool photons on the hot electrons of a completely ionized plasma. We present the best-fit parameters for the Comptonization model in Table 9.

This very high state has been observed (Miyamoto et al. 1991) in a few Galactic BHs. Yet another rubric for the very high state emerged in Kubota et al. (2001) and Kubota & Makishima (2004), where they identify this as the “anomalous” state, a state whose spectrum can be well fitted by a Comptonized scattering model. Regardless of the name, our best-fit Comptonization sources likely fit into this category. The luminosities of these sources suggest that they are stellar mass BH systems in this anomalous/very high state.

As with the low state, we include mass estimates for our high-state objects in Table 3. We assume that the high-state objects are radiating at L_{Edd} , resulting in a minimum mass if there is no beaming. We find masses of 1.6–38 M_\odot , consistent with “normal” stellar mass BHs, for the sources well fitted by the Comptonization model. The other high-state ULX masses range from 17 to 1350 M_\odot based on Eddington rates, analogous to the low-state ULX masses computed.

It is important to note that the initial simulations and discussions in Appendix A need to be considered in relation to the impact they pose to our classification scheme and the results presented in these sections. While it is indeed possible that some of the objects with a weak blackbody component and a relatively small number of counts would be miscategorized as a pure power-law spectrum, one can ask what such a possible situation would do to the correlations that we have seen. These putative objects, by assumption, would have lower luminosities; however, their temperatures are unknown and it is entirely unclear if they would destroy the kT/L_X correlation. As we have shown in our simulations, it is unlikely that the fitted power-law index would change, and thus the presence of a low state as indicated by the spectral index would not change. This would create a new type of object, one with a flat power law and a blackbody component, which is not seen in the Milky Way, nor among the high-S/N objects.

4.4. Temperature Gap

In addition to the existence of ULXs with low blackbody temperatures, the temperature distribution of the high-state (thermal dominated) ULXs (Fig. 5, *left panel*) displays a “gap” that is of particular interest: there is a complete absence of objects with

temperatures in the range 0.26–0.50 keV. It is tempting to take this as evidence for a gap in the mass distribution of these accreting BHs. Since, for a given luminosity, we expect the temperature to vary as $T \propto L^{1/4} M^{-1/2}$, this factor of 2 gap in the temperature distribution translates into a factor of 4 gap in the BH mass distribution.

If this result is borne out by further study, it provides an important clue to the origin and evolution of IMBHs. One popular idea is that IMBHs formed from the collapse of massive Population III stars (Madau & Rees 2001). Models suggest that Population III stars with zero-age main-sequence (ZAMS) masses in the range 25–140 M_\odot and above 260 M_\odot collapse to produce BHs (Heger & Woosley 2002), whereas in the range of ZAMS masses 140–260 M_\odot , pair instability supernovae lead to the complete disruption of the stars (i.e., no remnant BH remains). Hence, this model for IMBH formation predicts a gap in the IMBH initial mass function in the range of approximately 60–200 M_\odot (although this is uncertain on the low end due to the effect of the pulsational pair instability on the precollapse core). One possibility is that the gap in our observed temperature distribution (and hence the inferred gap in the mass function) is due to this effect of the pair instability supernovae in Population III stars. This would require that the current IMBH mass function is approximately the same as the initial IMBH mass function. In other words, it requires that most IMBHs (especially those just below the gap) have not grown significantly due to accretion since their formation and, hence, that the ULX phase represents a short fraction of the lifetime of an IMBH ($f \ll t_{\text{sal}}/t_{\text{H}}$, where $t_{\text{sal}} \approx 45\epsilon_{0.1}$ Myr is the e -folding timescale for Eddington-limited BH growth with radiative efficiency $\epsilon = 0.1\epsilon_{0.1}$).

An alternative interpretation of the inferred mass gap is to suppose that two fundamentally different modes of formation lead to a strong bimodality in the final BH mass function. BH masses below the gap can be readily understood through normal stellar processes. A separate and distinct population of significantly more massive BHs may result from dynamical processes in the core of dense globular clusters (Miller & Hamilton 2002; Gültekin et al. 2004).

4.5. Comparison with Galactic High-Mass X-Ray Binaries

Supposing that the Galaxy’s bright X-ray population is representative of low-redshift galaxies, we expected to find a number of sources similar to Galactic X-ray binaries in our sample. In our sample, we find approximately 24 sources with luminosities below our high-state ULX cutoff ($\approx 3 \times 10^{39}$ ergs s^{-1}), X-ray positions within the optical extent of their host galaxy, and no obvious optical counterpart. The unabsorbed luminosities for these sources are in the range $(0.4\text{--}2.5) \times 10^{39}$ ergs s^{-1} (0.3–10 keV band). Two of these sources were transients in the *XMM-Newton* data. Of the four host galaxies with multiple observations examined, two of these galaxies contained solely ULX sources in our luminosity regime (Holmberg II and NGC 5204). Each of the remaining two (NGC 253 and NGC 4258) had a transient source best fitted by a combined blackbody and a power law.

This suggests an interesting diagnostic in terms of distinguishing our ULX sources from a normal high-mass X-ray binary (HMXB) population. In our own Galaxy, most HMXBs vary on timescales of days or less and most of the BHs in the Milky Way are transients, although some HMXBs are indeed persistent. The figures in Kalogera et al. (2004), determined through detailed mass transfer calculations, indicate that transient behavior should not be expected from a population of IMBHs. Thus, on average, our ULX sources should remain X-ray bright in multiple observations. Through a literature search, we found that

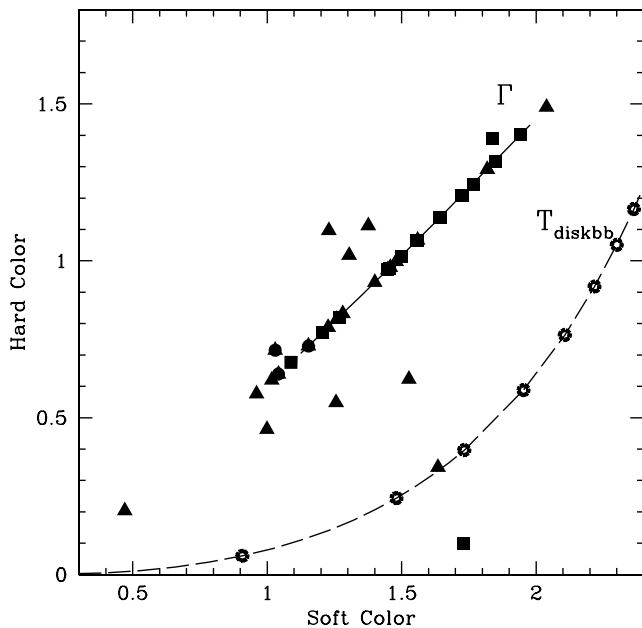


Fig. 6.—Color-color diagram plotting soft vs. hard colors, as outlined in Done & Gierlinski (2003), for low-state (rectangles) and high-state (triangles) ULXs. The filled circles represent the sources with low $\Delta\chi^2$ values between the two-component and power-law models. A large number of our sources lie in the same range of this graph as the BH sources examined by Done & Gierlinski (2003) (near the power-law distribution, indicated by the solid line). The dashed line represents the color-color plot for a multicolored disk model with different disk temperatures. The sources approaching this line were those well fitted by the Comptonization model. Done & Gierlinski (2003) had no BH sources in this region, but atolls and Z sources, which were also well fitted by Comptonization models.

37/42 of our ULX sources are well detected in *Röntgensatellit* (*ROSAT*) observations and thus are luminous for greater than 10 yr and therefore are not transients. Examination of the long-term light curves shows that most of these sources vary by less than a factor of 3 over the timescale from *ROSAT* to *XMM-Newton*. The sources that have been above the Eddington limit in the Milky Way and the Magellanic Clouds do so transiently, for a small fraction of the time. As best as we can tell, from the light curves from *Einstein*, *ROSAT*, *ASCA*, *Chandra*, and *XMM-Newton* the ULXs are rarely transients and are almost always “on,” unlike Galactic “ultra-luminous” objects.

As a possible further diagnostic, we constructed a color-color diagram for our ULX sources. We adopted the colors of Done & Gierlinski (2003) in order to compare our sample with their sample of Galactic X-ray sources. Thus, our colors were constructed from unabsorbed model fluxes in four energy bands: 3–4, 4–6.4, 6.4–9.7, and 9.7–16 keV. The XSPEC command `dummyresp` was used to calculate a flux based on the model for the 10–16 keV range. We plot colors for a pure unabsorbed power law (from $\Gamma = 1.5$ –3.0) and an unabsorbed MCD model (`diskbb` in XSPEC with $kT_{\text{in}} = 5.0$ –0.2 eV) for comparison. Comparing our Figure 6 with Figure 8 of Done & Gierlinski (2003), we find that our ULX sources largely lie along the same regions as their BH sources. A few ULX sources, however, lie in the region occupied by atoll and Z sources in the plot of Done & Gierlinski (2003). These sources were those best fitted by a Comptonization model.

4.6. Galaxy Sample

In this section we examine the environment in which ULX sources reside. We investigate the claim that the ULX population is proportional to the host galaxy’s star formation rate (SFR;

Ranalli et al. 2003; Grimm et al. 2003). Toward this end, we use the far-infrared luminosity of the host galaxy as an indicator of the SFR. In order to compare the ULX population of a galaxy with the SFR, we followed a similar approach to Swartz et al. (2004). We calculate the FIR flux from observations taken by the *Infrared Astronomical Satellite* (*IRAS*). As in Swartz et al. (2004), the flux between 42.4 and 122.5 μm is approximated as $1.26 \times 10^{-11}(2.58S_{60} + S_{100})$ ergs $\text{cm}^{-2} \text{s}^{-1}$. The values of the flux at 60 μm (S_{60}) and 100 μm (S_{100}) were obtained from either Ho et al. (1997) or NED. Luminosities were calculated using the distances quoted in Table 1. We list these values in addition to the number of ULXs observed in individual galaxies in Table 10. The number of ULXs includes both the objects we classify as high- and low-state ULXs and those sources resolved by *Chandra*.

In Figure 7 we show two plots relating the number of ULXs to L_{FIR} . It has been suggested by Grimm et al. (2003) that the luminosity function in the X-ray regime from HMXBs is related to SFR. In the left panel we find that the galaxies with the highest L_{FIR} seem to have fewer ULXs than may be expected from the luminosity functions of Grimm et al. (2003), who present a relationship showing a scaling of the number of HMXBs with luminosities over a set threshold with the host galaxy’s SFR (see eq. [7] of Grimm et al. 2003). Using this relationship, we would expect a galaxy with an SFR approximately equal to that of M51 ($\approx 4 M_{\odot} \text{yr}^{-1}$ from their Table 1) to have ≈ 4.47 objects with luminosities greater than 10^{39} ergs s^{-1} . We find five objects with this luminosity in M51, consistent with their result. However, for NGC 4945, a galaxy with approximately the same L_{FIR} and therefore SFR, we find only one source with a luminosity in this range. However, we note that NGC 4945 is a Seyfert, implying that the L_{FIR} may primarily be caused by the AGN and not a direct indication of SFR. In addition to high L_{FIR} sources with few ULXs, we find a number of sources with very small SFR but that contain a ULX. For sources with SFR $< 0.2 M_{\odot} \text{yr}^{-1}$, which corresponds roughly to sources with L_{FIR} less than that of NGC 4736, we would expect < 0.22 sources with luminosities above 10^{39} ergs s^{-1} . However, there are a number of bright ULXs in galaxies with very low SFRs (for instance, Holmberg II, Holmberg IX, NGC 5204, and NGC 5408). Thus, in a direct comparison, our results do not agree with the predictions of Grimm et al. (2003).

The right panel displays the average number of ULXs per galaxy, binned according to luminosity. This plot is extremely similar to Figure 15 of Swartz et al. (2004) for spiral galaxies. Thus, once again, it seems that the connection between SFR and the ULX population in spiral galaxies is supported. For irregular galaxies, however, there seems to be more of a spread in the distribution. This could be the result of poor sampling: most of the bins contain only one galaxy. Another possibility is that there is no direct correlation in irregular galaxies or that the overall star formation in these galaxies is less ordered or clumpier. If the latter is the case, the overall SFR of the galaxy is only an average over a wide range of values. We will address this issue again in the next paper in this series (Winter et al. 2005), where we discuss the local environments of the ULXs in our sample.

In Figure 8 we plot the distribution of column densities among the ULXs. We subtracted the Galactic column density toward the galaxy (obtained from the `nH FTOOL` and listed in Table 1) from the values obtained through spectral fits. We note that, on average, the ULXs have large column densities. The typical Galactic column density along a line of sight is $\approx 4 \times 10^{20} \text{cm}^{-2}$. If the ULX is located on the opposite side of its host galaxy, we might expect maximum column densities of $\approx 1.2 \times 10^{21} \text{cm}^{-2}$. However, most of our sources have column densities well above this

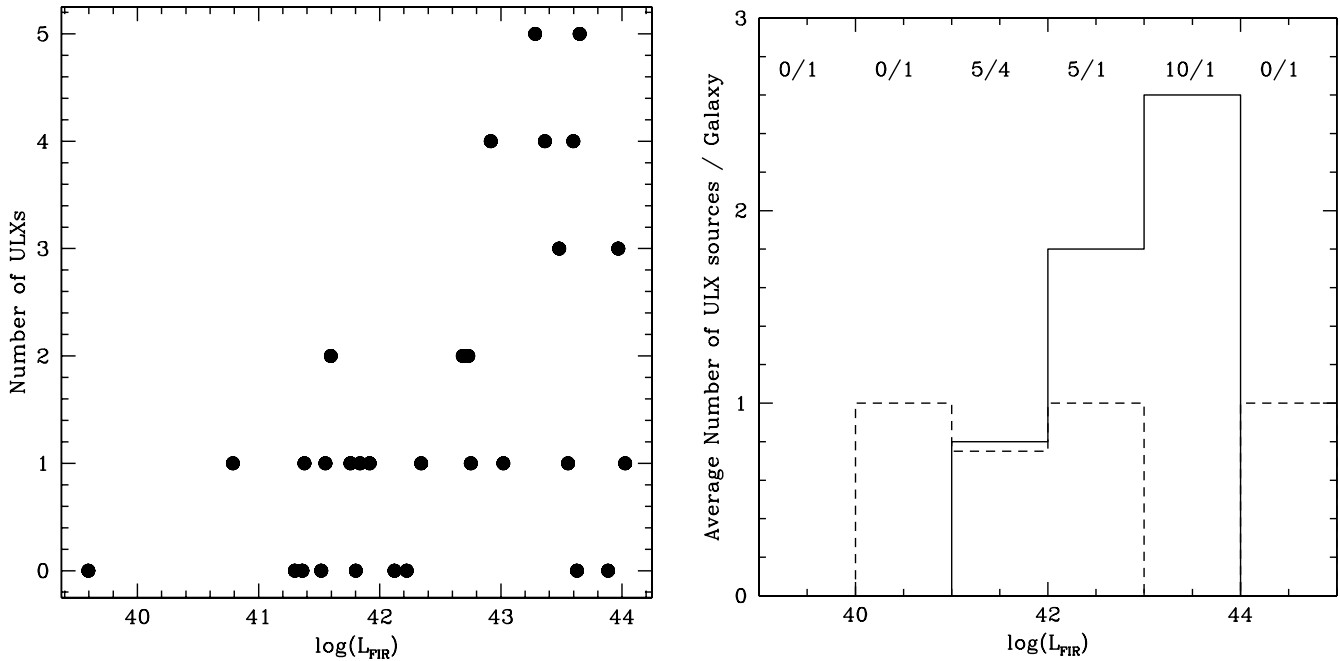


FIG. 7.— *Left*: Relationship of the far-infrared luminosity, as an indicator of SFR, vs. the number of ULXs for each galaxy. If ULXs are associated with star formation, we naively expect that the higher the FIR luminosity the more ULXs the galaxy will host. *Right*: The distribution of average number of ULXs per L_{FIR} bin for spiral galaxies (solid line) follows this expectation. The distribution of irregular galaxies (dashed line) is not so easily interpreted. The numbers at the top indicate the number of spiral/irregular galaxies in each of the luminosity bins. More irregular galaxies would need to be included in this survey for meaningful statistics on this group.

value. This is in agreement with the analysis of five ULXs by Roberts et al. (2004) and may imply, as they suggest, that the local environment of the ULXs contains an extra source of absorption. We are investigating this further, comparing the X-ray absorption column densities with H I data (Winter et al. 2005).

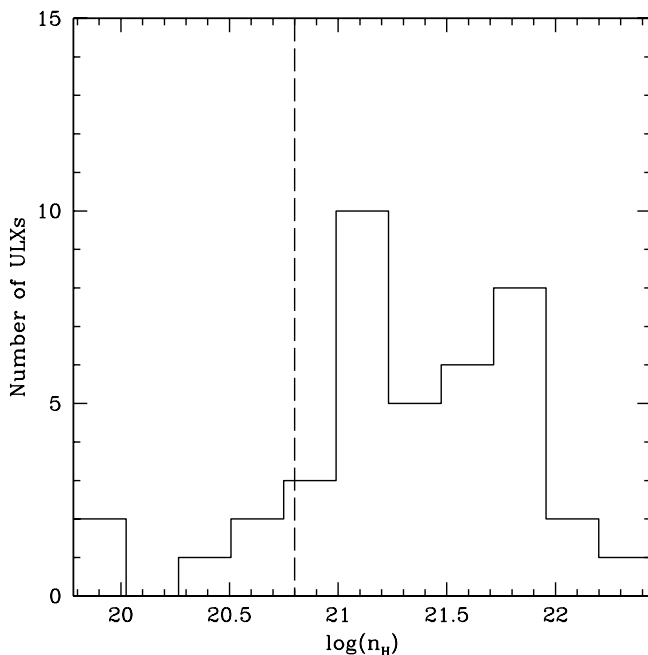


FIG. 8.— Distribution of the hydrogen column densities of ULX sources. The n_{H} values were obtained through spectral fits using the wabs model in XSPEC. Galactic column densities toward the host galaxy were subtracted from the spectral fit values. A majority of our ULX sources have high column densities ($>10^{21} \text{ cm}^{-2}$), suggesting that some of this absorption originates with the local ULX environment. Bins to the left of the dashed line represent sources with column densities very close to the Galactic value, and thus a simple subtraction is not statistically representative of the true value.

In order to better understand the relationship between SFR and the ULX population, it is necessary to extend ULX studies to other wavelengths. In particular, it becomes important to analyze UV and IR images close to the ULX.

5. CONCLUSIONS

We present the results of an *XMM-Newton* survey of the ULX population in nearby galaxies. In this study we assumed that ULXs are isotropic emitters. For our selected ULX sources (which excluded transient sources and supernovae), this assumption was supported by the finding that 37/42 of our ULXs were found to be “on” in *ROSAT* observations. This implies that these sources exhibited high luminosities for timescales of at least 10 yr, a property that is not seen in Galactic Eddington limit–exceeding sources (such as BH X-ray binaries undergoing an outburst). We also assumed that if some ULX sources represent a class of IMBH X-ray binaries, they would exhibit spectral states analogous to Galactic stellar mass BH X-ray binaries. This is the hypothesis we set out to test, classifying a source as a ULX based on (1) spectral form, (2) luminosity, and (3) coincidence of the X-ray source within the optical host galaxy. Due to the quality of spectra available for these distant X-ray sources, our classification of spectral form is really a first approximation describing the basic curvature of the spectrum.

Through this study we have found that there exists a population of objects whose X-ray spectral properties closely match the low/hard-state spectra of Galactic BHs, but whose luminosities lie in the range of $L_{\text{bol}} \approx 2 \times 10^{38} - 1 \times 10^{40} \text{ ergs s}^{-1}$. In the Milky Way, BHs with these spectral properties radiate at only ≈ 0.05 of the Eddington limit. If this is also true for this population, it indirectly implies that these objects have a mass greater than $\approx 30 M_{\odot}$ ranging up to $1500 M_{\odot}$ and thus should be IMBHs. The existence of such objects was “predicted” on the basis that the ULXs previously studied shared the X-ray spectral characteristics of high-state Galactic BHs, namely, an X-ray spectrum best fitted by a combined blackbody and a power law (Miller et al.

2003), but with much higher luminosities. If these objects are high-state IMBHs, the corresponding low-state objects should also exist.

Our survey has also uncovered a large population of objects whose X-ray spectra are well modeled by the canonical description of Galactic BHs in the high state (thermal dominated), a BH with a steep power law, but whose bolometric luminosities exceed 2×10^{39} ergs s⁻¹, ranging up to $10^{41.5}$ ergs s⁻¹, and whose blackbody temperatures are less than 0.3 keV. If these objects are radiating at $\approx \frac{1}{2}$ the Eddington limit like their Milky Way counterparts, their implied masses are 30–3000 M_{\odot} , a range very similar to that implied by the low-state objects. Using the $M^{-1/4}$ scaling of mass to temperature, the observed spectral temperatures give masses of 500– $10^4 M_{\odot}$, a considerably larger value. In general agreement with the expectations of the IMBH hypothesis, the objects with high-state spectra are more luminous than those with low-state spectra. We note that these results have required the high S/N of *XMM-Newton* in order to discern the spectrum of these objects. Many of these objects have also been observed by *Chandra*, and their spectra have been well fitted by simple power laws.

In addition to classification of the sources, we investigated some of the properties of the ULX sources. We found a gap in the temperature distribution of high/soft-state ULXs. This gap may indicate a gap in mass distribution, which may provide clues to the nature of ULXs. We also found that our ULXs are persistent sources (not transients) that occupy regions on the color-color diagram of Done & Gierlinski (2003) also occupied by Galactic

BH sources. Finally, the existence of a substantial population of ULXs in nearby dwarf and other low SFR galaxies argues that (in agreement with Ptak & Colbert 2004; Swartz et al. 2004) there is more than one source term for the origin of ULXs, with at least some of them not being associated with recent star formation, at least statistically.

We conclude, from an X-ray spectral and luminosity point of view, that our data are consistent with many of these objects having the properties expected of an IMBH population. However, we also find two other populations of objects, those whose blackbody temperature and luminosity correspond to that of stellar mass BHs with $kT \approx 1$ keV and $\log L_X$ less than 2×10^{39} ergs s⁻¹, and a small population of objects whose X-ray spectra and luminosities are consistent with that of stellar mass BHs in the very high state. Thus, ULXs selected purely on the basis of 0.3–10 keV X-ray luminosities are a composite class with $\approx \frac{1}{4}$ being “normal” stellar mass BHs and the rest being consistent with a population of IMBHs.

In a follow-up paper we will discuss the environments of these objects as revealed by *XMM-Newton* OM UV imaging and the implications this has for the origin of ULXs.

L. W. gratefully acknowledges Kip Kuntz and M. Coleman Miller for helpful discussions. We would also like to acknowledge R. Narayan for asking the question “are there any low-state ULXs?” at the Kyoto Black Hole meeting.

APPENDIX A

SPECTRAL SIMULATIONS

A1. TWO-COMPONENT MODEL

In order to determine the number of counts required to distinguish whether a blackbody component is statistically significant for the sources fitted with a two-component model, we simulated spectra based on that of some of the brightest sources. We chose to simulate spectra of bright two-component spectra exhibiting three different cases: (1) the flux from the blackbody dominates over the power-law component at $2kT$, (2) an intermediary case, and (3) the flux from the power law dominates over the blackbody component at $2kT$. Such simulations would allow us to determine the uncertainty in our claims of a combined fit being a better descriptor of the data. This is necessary because there is no a priori model that predicts the relative intensities of the two components and, as we know from studies of Galactic BHs, these components show a wide variety of relative intensities. To this end, we simulated spectra using the best-fit absorbed blackbody and power-law model with the `fakeit` command in XSPEC. We chose (1) NGC 247 XMM1, (2) NGC 5408 XMM1, and (3) Holmberg II XMM1 as our seed observations. These objects all have very high S/N and thus the fits are robust. The respective ratios of power-law flux to blackbody flux contributions at $2kT$ are (1) $\ll 1.0$, (2) 1.77, and (3) 3.52. All of these sources have comparable blackbody temperatures indicative of our high-state ULX candidates (roughly $kT \approx 0.15$).

We simulated 500 spectra each, using the two-component model, for each of 2000, 1000, 400, and 200 counts for the PN. Each simulated spectrum, based on the best-fit blackbody and power-law model, was fitted with an absorbed blackbody and power-law model and an absorbed pure power-law model. We placed the constraint that the blackbody temperature must lie within the range of 0.07–4.0 keV (the range at which it would be detectable in the *XMM-Newton* bandpass). We allowed the power-law index to vary over the range 0–4 for the power-law component of the combined blackbody and power-law model. However, we placed a constraint that the power-law component must lie within the range $\Gamma = 1.5$ –2.0 for the simple power-law model to be consistent with our fits to the sources we claim are best fitted by simple power laws. This constraint ensures that the spectral index would exhibit that of our classified “low-state” objects.

When analyzing and classifying our real spectra, we declared a detection of the thermal disk component if the addition of this component (to a baseline power-law model) led to an improvement of the goodness-of-fit parameter by at least $\Delta\chi^2 = 8$. We can use the above simulations to address the detectability of a thermal disk component using this $\Delta\chi^2$ threshold as a function of the relative strength of the thermal component and the number of counts in the spectrum. For each simulation, we fit the spectrum with both a single absorbed power-law and a two-component power-law and thermal disk model and compute the quantity $\Delta\chi^2 = \chi_{\text{pow}}^2 - \chi_{\text{pow+disk}}^2$. In Figure 9 we plot the distribution of $\Delta\chi^2$ from our 500 simulations for the weak and strong blackbody component for spectra with 400 and 2000 counts. It is clear that we cannot detect a weak thermal component in a 400 count spectrum: the vast majority of the simulations ($\approx 82\%$) result in $\Delta\chi^2 < 8$. However, even a weak thermal component is easily detected in a 2000 count spectrum (not a single simulation gave $\Delta\chi^2 < 8$). The strong blackbody case is detectable with high significance even in a 400 count spectrum ($< 1\%$ of the simulations resulted in $\Delta\chi^2 > 8$).

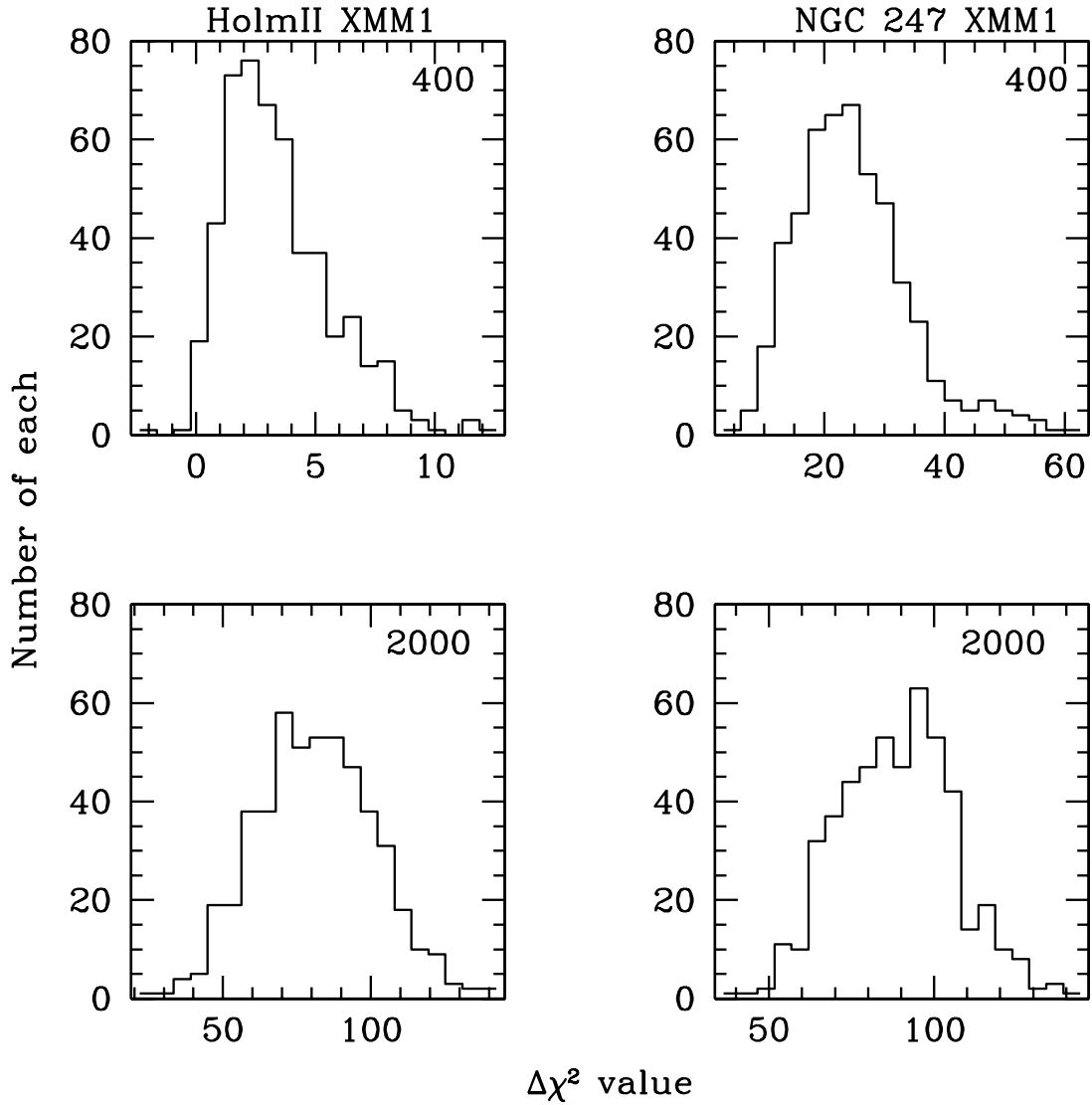


FIG. 9.—Distribution of $\Delta\chi^2$ from simulations. The $\Delta\chi^2$ values represent the difference between the unreduced χ^2 of the absorbed power-law model and the combined blackbody and power-law model. *Left*: Results for the “weak” blackbody component relative to power law for 500 simulated spectra at 400 counts (*top*) and 2000 counts (*bottom*). *Right*: Results for the “strong” blackbody component. For a weak blackbody component at 400 counts, the thermal component is undetectable. However, it is able to be distinguished as the number of counts is increased. A strong blackbody component is easily distinguishable at 400 counts.

When we increase the upper limit of the range of the spectral index in XSPEC for the power-law model to $\Gamma = 3.0$, our confidence levels decrease. For a weak thermal component with 400 counts, all of the simulations result in $\Delta\chi^2 < 8$. At 2000 counts, only $\approx 30\%$ of the simulations for a weak thermal component have $\Delta\chi^2 < 8$. For a strong thermal component, 20% of the simulations yield $\Delta\chi^2 < 8$ for 400 counts while, as was the case for $\Gamma = 2.0$, none of the simulations gave $\Delta\chi^2 < 8$ for 2000 counts.

Thus, allowing the Γ to “float freely” or remain unconstrained further decreases the confidence levels. When the Γ parameter is allowed to float, the spectra are fitted with higher Γ -values in order to compensate for the missing blackbody component. When the upper limit was instituted at 2.0 or 3.0, we found that all 500 simulated spectra were fitted with a $\Gamma = 2.0$ or 3.0, respectively, for the simple power-law model. This same affect is not seen in the Γ of the two-component model, where the value ranges between 1.4 and 4.0 with a peak in the distribution near that of the original model used to simulate the spectra. Thus, higher power-law indices (>3.0) can indicate the necessity of an added blackbody component. Since there are no Galactic BHs whose broadband spectra are well fitted by steep power laws, it seems that restricting the allowed power-law indices is more consistent with the nature of Galactic BHs. In fitting our sources with the three standard models, we allowed the Γ to float; thus, the problem of a missing blackbody component being compensated for by a steep power law should not have factored into our classification criteria.

A2. SIMPLE POWER-LAW MODEL

Our next set of simulations sought to determine our confidence in the simple power-law fit being an adequate descriptor of the spectra. Binning provides a problem in distinguishing between a power law and a curvature in the spectrum at the low-energy range, since the binning procedure can wash out a low- kT blackbody from the spectrum. For this reason, we chose to simulate unbinned PN spectra for a source we categorized as a low-state object, IC 0342 XMM1. IC 0342 XMM1 represents characteristics typical of our low-state

candidates, namely, it is within the proper luminosity range and it has a power-law index of $\Gamma \approx 1.7$ (the median of the distribution for low-state objects is 2.03) and a hydrogen column density near the median of all of the fitted values (where the median value is $\approx 3 \times 10^{21} \text{ cm}^{-2}$ and the value of IC 0342 X-1's column density is $5.8 \times 10^{21} \text{ cm}^{-2}$). We chose this source for these reasons and the high number of counts in its PN spectrum. Instead of using the χ^2 statistic (used for binned data), we chose to use the maximum likelihood statistic, *C-stat*, in XSPEC (which uses unbinned data).

We simulated 500 spectra using the best-fit parameters for the simple power-law fit using the *fakeit* command. We fitted the simulated spectra with two models, the simple power-law model and a combined blackbody and power-law model, and computed the change in the goodness of fit, $\Delta\chi^2$. For the two-component model, once again we placed the constraint that the blackbody temperature remain in the range that it would be detectable by *XMM-Newton*, 0.07–4 keV. We followed this procedure for 1000, 2000, and 4000 counts. At both the 1000 and 2000 count level, the addition of a second component has no effect on the *C*-statistic (the distributions in *C*-space for both the power-law fit and the two-component fit are indistinguishable).

At the 4000 count level, the *C*-statistic distributions for the two models separate such that there is a 26% confidence that the two-component model is a better fit to the data. We find, when we examine the model parameters, that the power-law index (Γ) for the two-component model ranges between 1.19 and 2.12 with the mean value ≈ 1.74 . The mean value for all three count levels used clustered around this value, although the range in Γ increased as the counts decreased. The mean blackbody temperature for simulations with 4000 counts was 1.17 keV (with the range varying between the amount previously noted) with a median of 1.06 keV. For simulations with lower counts, the blackbody temperature becomes higher (1.24 keV for 1000 counts) with a higher median (1.83 keV for 1000 counts). This tells us that the fitting procedure tends to approximate a pure power-law spectrum as a two-component spectrum with Γ equal to that of the true spectral index but with a blackbody temperature higher than those observed in our study (1.1 keV or higher), which in the *XMM-Newton* band can be approximated as a power law. If we found spectra in our sample that were best fitted with a low spectral index and a high blackbody temperature, we might suspect that the spectrum's true nature is a power law. We also note that if the hydrogen column density is large, much greater than $3 \times 10^{21} \text{ cm}^{-2}$, a low-temperature (kT) blackbody component can be much more difficult to detect.

APPENDIX B

ADDITIONAL SPECTRAL FITS

The following sources were not best fitted by the standard models employed in this study.

B1. NGC 300 XMM4

This source was classified as a supersoft X-ray source by Kong & Di Stefano (2003). We find that the standard single-component absorbed blackbody model is a much better model for this spectrum. In fact, the power-law, bremsstrahlung, and combined models do not fit the data within the 90% confidence range. Fitting an absorbed blackbody, we find that the best fit corresponds to the following parameters: $n_{\text{H}} = 1.38_{-0.55}^{+0.27} \times 10^{21} \text{ cm}^{-2}$, $kT = 0.059_{-0.005}^{+0.007} \text{ keV}$, and $\chi^2/\text{dof} = 74.5/45$. This fit yields an unabsorbed flux of $3.3 \times 10^{-13} \text{ ergs cm}^{-2} \text{ s}^{-1}$.

B2. NGC 4631 XMM4

The spectrum of this source clearly identifies it as a supersoft X-ray source. As with NGC 300 XMM4, the standard models employed in this study did not adequately match the data. The best-fitting model corresponds again to an absorbed blackbody. The corresponding parameters are as follows: $n_{\text{H}} = 6.2_{-1.5}^{+0.26} \times 10^{21} \text{ cm}^{-2}$, $kT = 0.07_{-0.01}^{+0.01} \text{ keV}$, and $\chi^2/\text{dof} = 142.3/74$. This fit yields an unabsorbed flux of $9.5 \times 10^{-12} \text{ ergs cm}^{-2} \text{ s}^{-1}$. The position of this source shows it to be coincident with a globular cluster associated with that galaxy. This source was identified as a bulge X-ray source, possibly powered by accretion, in a *ROSAT* study of NGC 4631 (Vogler & Pietsch 1996).

B3. NGC 4631 XMM5

The spectrum of this source was best fitted with an absorbed power-law plus an absorbed vapec model. This indicates the presence of hot gas, indicating a possible thermal X-ray source.

B4. NGC 4945 XMM5

The spectrum of this source was not adequately fitted with any of the standard models used in this investigation. The spectrum exhibits a prominent Fe K line in the PN spectrum that is well fitted by a Gaussian (*zgauss*) at 6.4 keV. We find that the entire spectrum is best fitted with a partial covering fraction absorption model (*pcfabs*) in combination with the normal absorption, a power law, and a Gaussian. The best-fit parameters yield absorption column density, $n_{\text{H}} = 1.79 \times 10^{21} \text{ cm}^{-2}$, partial covering absorption, $n_{\text{H}} = 18.4 \times 10^{21} \text{ cm}^{-2}$, partial covering fraction of 0.82, $\Gamma = 1.6$, and $\chi^2/\text{dof} = 61.8/57$. The source is clearly located within the optical galaxy and is thus unlikely to be a background AGN.

B5. M51 XMM5

The spectrum and luminosity ($L_{\text{X}} \approx 1.9 \times 10^{42} \text{ ergs s}^{-1}$) of this source suggest that it is an AGN. The location of the source, from the DSS, places it within the dwarf companion of M51, making a value of the optical flux hard to constrain. The best fit to this source was an absorbed blackbody plus power law, and the spectral parameters are listed in Table 4.

B6. M83 XMM2

Like NGC 4945 XMM5, this source was best fitted by a partial absorption model. However, this source showed no evidence of an Fe K line. We fit this source's spectra using a partial covering fraction absorption model in combination with the normal absorption model and a power law. The best-fit parameters yield absorption column density, $n_{\text{H}} = 2.1 \times 10^{21} \text{ cm}^{-2}$, partial covering absorption, $n_{\text{H}} = 43.5 \times 10^{21} \text{ cm}^{-2}$, partial covering fraction of 0.86, $\Gamma = 2.95$, and $\chi^2/\text{dof} = 83.5/84$. The unabsorbed flux in the range of 0.3–10 keV equals $1.37 \times 10^{-12} \text{ ergs cm}^{-2} \text{ s}^{-1}$.

B7. INVERSE COMPTON SCATTERING SOURCES

Table 9 includes the parameters for the ULX sources best fitted by the compST model. A discussion of these sources and interpretation of the data are included in § 4.3.

APPENDIX C

ADDITIONAL TABLES

In this appendix we include additional tables containing supporting material for the text of the paper. In Table 6 we list details of the *XMM-Newton* observations for all of the point sources examined in this study. Table 7 lists information for bright sources that we excluded from our study, due to their classification as either foreground stars or background AGNs. Table 8 includes single-component (absorbed power law) model fits for the sources listed in Table 4, while Table 9 includes Comptonization model fit parameters for the sources mentioned in § 4.3 (possible very high state stellar mass black holes with luminosities in the ULX regime). Finally, Table 10 includes the IR flux information for ULX host galaxies used to construct Figure 7.

TABLE 6
BRIGHT POINT SOURCES EXAMINED

| Source ^a | R.A. | Decl. | Total Counts | Count Rate ^b (10^{-2} counts s^{-1}) | ID | Location in Galaxy ^c | <i>XMM-Newton</i> References ^d |
|---------------------------------|------------|-------------|-------------------|---|---------------------------------|------------------------------------|--|
| NGC 247 XMM1 | 00 47 03.8 | −20 47 46.2 | 3458, 1389, 1379 | 20.33, 5.8, 6.4 | 1RXS J004704.8–204743 | sa | |
| NGC 247 XMM2 | 00 47 03.1 | −20 37 02.5 | ..., 597, 600 | ..., 1.9, 1.4 | ... | sa | |
| NGC 253 XMM1 | 00 47 32.8 | −25 17 52.6 | ..., 3156, 2985 | ..., 11.38, 9.9 | NGC 253 PSX-2 ^e | Near center | 1 |
| ... | ... | ... | ..., 12654, 12812 | ..., 8.7, 9.1 | ... | ... | |
| NGC 253 XMM2 | 00 47 22.4 | −25 20 55.2 | ..., 825, 942 | ..., 2.8, 2.97 | NGC 253 PSX-5 | sa | 1 |
| ... | ... | ... | ..., 10347, 10304 | ..., 8.2, 8.5 | ... | ... | |
| NGC 253 XMM3 | 00 47 35.2 | −25 15 13.8 | ..., 870, 1065 | ..., 3, 3.41 | NGC 253 PSX-7 | sa | 1 |
| ... | ... | ... | ..., 5988, 6131 | ..., 4.2, 4.6 | ... | ... | |
| NGC 253 XMM4 | 00 47 23.3 | −25 19 06.5 | ..., 649, 703 | ..., 1.4, 1.3 | ... | sa | |
| ... | ... | ... | ..., 3823, 3738 | ..., 1.7, 1.95 | ... | ... | |
| NGC 253 XMM5 | 00 47 17.6 | −25 18 12.1 | ..., 295, 313 | ..., 1.08, 1.04 | NGC 253 PSX-4 | sa | 2 |
| ... | ... | ... | ..., 4199, 4303 | ..., 3.6, 3.8 | ... | ... | |
| NGC 253 XMM6 | 00 47 42.8 | −25 15 05.5 | ..., 6081, 6407 | ..., 3.8, 4.4 | NGC 0253 [VP99] X40 | sa | 1 |
| NGC 253 XMM7 ^f | 00 47 09.2 | −25 21 21.7 | ..., 4300, 4454 | ..., 2.6, 3.0 | ... | sa | |
| NGC 300 XMM1 | 00 55 09.9 | −37 42 13.9 | 6778, 2248, 2453 | 18.6, 4.9, 5.4 | ... | sa | |
| NGC 300 XMM2 | 00 55 10.6 | −37 48 36.7 | 1364, 456, 463 | 3.1, 0.9, 0.9 | ... | Edge sa? | |
| NGC 300 XMM3 | 00 54 49.7 | −37 38 53.8 | 915, 442, 435 | 2.2, 0.9, 0.9 | ... | sa ^g | |
| NGC 300 XMM4 | 00 55 10.9 | −37 38 53.8 | 745, 224, 233 | 1.9, 0.3, 0.4 | XMMU J005511–3749; SSS | sa | 3 |
| NGC 300 XMM5 | 00 55 21.1 | −37 29 19.5 | 750, 247, 250 | 1.7, 0.4, 0.5 | ... | Out | |
| NGC 300 XMM6 | 00 54 44.2 | −37 51 04.5 | 517, 187, 165 | 1.1, 0.3, 0.3 | ... | Out | |
| NGC 625 XMM1 ^h | 01 35 06.8 | −41 26 17.1 | 5832, 577, 2119 | 3, 0.6, 1.4 | ... | sa | |
| NGC 1313 XMM1 | 03 18 19.9 | −66 29 10.7 | 2876, 900, 810 | 8.6, 3.2, 2.8 | NGC 1313 [CPS95] X-1; IXO 07 | sa | 4,5 |
| NGC 1313 XMM2 | 03 17 38.8 | −66 33 05.3 | 7568, 2357, 2108 | 25.4, 8.8, 7.8 | NGC 1313 [CPS95] X-3; SN 1978 K | Edge sa | 6 |
| NGC 1313 XMM3 | 03 18 22.5 | −66 36 06.2 | 6960, 2179, 1793 | 23.3, 8.1, 6.6 | NGC 1313 [CPS95] X-2; IXO 08 | Edge sa? | 4,5 |
| NGC 1313 XMM4 | 03 18 18.5 | −66 30 05 | 2075, 659, 567 | 5.1, 1.8, 1.5 | NGC 1313 [SPC2000] X-8 | Near center | |
| IC 0342 XMM1 | 03 45 55.8 | +68 04 54.5 | 1802, 1216, 1105 | 33.6, 12.4, 11.1 | IC 0342 [RW2000] X-1; IXO 22 | sa | 5, 7, 8 |
| IC 0342 XMM2 | 03 46 15.0 | +68 11 11.2 | 1147, 541, 184 | 21.1, 5.5, 1.7 | IC 0342 [RW2000] X-3 | sa | 7, 8 |
| IC 0342 XMM3 | 03 46 48.6 | +68 05 43.2 | 1186, 670, 606 | 21.7, 6.8, 6.0 | IC 0342 [LLJ2000] X-2 | Near center | 7, 8 |
| IC 0342 XMM4 | 03 46 57.2 | +68 06 20.2 | 551, 338, 377 | 9.5, 3.9, 3.6 | IC 0342 [RW2000] X-6 | Near center | 7, 8 |
| NGC 1569 ⁱ | ... | ... | ... | ... | ... | ... | ... |
| NGC 1705 XMM1 | 04 54 57.6 | −53 24 23.5 | 1174, 400, 371 | 2.4, 0.6, 0.6 | RX J0454.9–5324 | Out? | |
| NGC 1705 XMM2 | 04 54 19.6 | −53 20 41.9 | 933, 375, 397 | 1.9, 0.6, 0.6 | ... | Out? | |
| NGC 1705 XMM3 | 04 54 38.1 | −53 18 16.2 | 698, 372, 418 | 1.4, 0.6, 0.6 | WGA J0454.7–5318 | Out? | |
| Mrk 71 XMM1 | 07 28 51.8 | +69 07 27 | 832, 225, 207 | 3.9, 0.97, 0.9 | ... | Out | |
| NGC 2403 XMM1 | 07 36 25.6 | +65 35 40 | ..., 1199, 672 | ..., 1.0, 0.60 | NGC 2403 [RW2000] X-1 | Edge sa | |
| NGC 2403 XMM2 | 07 36 50.2 | +65 36 02.1 | 1964, 729, 672 | 1.99, 0.63, 0.60 | ... | Near center | |
| NGC 2403 XMM3 | 07 36 55.4 | +65 35 40.3 | 1497, 489, 378 | 1.4, 0.40, 0.33 | ... | Near center | |
| NGC 2403 XMM4 | 07 37 02.5 | +65 39 35.2 | 1004, 274, 288 | 0.52, 0.15, 0.21 | NGC 2403 [RW2000] X-4 | Edge sa? | |

TABLE 6—Continued

| Source ^a | R.A. | Decl. | Total Counts | Count Rate ^b (10 ⁻² counts s ⁻¹) | ID | Location in Galaxy ^c | <i>XMM-Newton</i> References ^d |
|----------------------------------|------------|-------------|-----------------------------|---|--|------------------------------------|--|
| Hol II XMM1 | 08 19 28.8 | +70 42 20.3 | 31052, 1257, 10807 | 272.2, 75.5, 72.7 | Holm II X-1; IXO 31 ^j | Near center? | 9 |
| | ... | ... | 3853, 1361, 1452 | 78.3, 18.9, 20.5 | ... | ... | |
| Hol I XMM1..... | 09 41 30 | +71 12 34 | 687, 768, 754 | 2.9, 2.7, 2.6 | ... | Out? | |
| Hol I XMM2..... | 09 39 59.7 | +71 06 40.2 | 575, 203, 224 | 2.5, 0.7, 0.7 | 1WGA J0940.0+7106 | Out? | |
| Hol I XMM3..... | 09 42 06.7 | +71 04 45.3 | 452, 141, 141 | 1.7, 0.4, 0.4 | ... | Out? | |
| M81 XMM1..... | 09 55 32.9 | +69 00 34.8 | 50788, ..., 18988 | 51.1, ..., 21.7 | NGC 3031 [RW2000] X-11 | sa | |
| | ... | ... | ..., 1227, ... ^k | ..., 12, 13.1 | ... | ... | |
| M81 XMM2..... | 09 55 24.8 | +69 01 11.7 | 17871, ..., 4121 | 13.2, ..., 4.4 | SN 1993J | sa | 10 |
| M81 XMM3..... | 09 55 10.6 | +69 05 02.2 | ..., ..., 1970 | ..., ..., 1.5 | NGC 3031 [RW2000] X-05 | sa | |
| M81 XMM4..... | 09 55 24.3 | +69 10 00.2 | ..., ..., 1197 | ..., ..., 1.0 | NGC 3031 [RW2000] X-08 | Edge sa | |
| M81 XMM5..... | 09 55 49.2 | +69 05 30.5 | ..., ..., 2077 | ..., ..., 2.3 | ... | sa | |
| M82 ^l | ... | ... | ... | ... | ... | ... | ... |
| Hol IX XMM1..... | 09 57 53.3 | +69 03 48.7 | 14976, 6546, 6586 | 207.3, 64.3, 65 | Hol IX X-1; IXO 34 | ? | 4, 5 |
| Sextans A XMM1..... | 10 11 24.6 | -04 42 17.2 | 3963, 1323, 1242 | 17.2, 5, 4.5 | ... | Out | |
| IC 2574 XMM1..... | 10 28 42.4 | +68 28 17.8 | 1047, 673, 623 | 8.3, 2.6, 2.5 | ... | sa | |
| IC 2574 XMM2..... | 10 26 33.5 | +68 29 32.1 | 533, 335, 300 | 4.3, 1.3, 1.2 | ... | Out | |
| IC 2574 XMM3..... | 10 27 22.2 | +68 18 47.6 | 538, 293, 301 | 4.2, 1.1, 1.2 | ... | Out | |
| NGC 4214 XMM1 | 12 15 37.0 | +36 19 29.4 | 434, 230, 225 | 2.9, 1.6, 1.5 | NGC 4214 [HSS2004] 11 | sa | |
| NGC 4214 XMM2 | 12 15 58.2 | +36 22 38.5 | 626, 160, 285 | 3.4, 0.6, 1.5 | ... | Out | |
| NGC 4258 XMM1 ^f | 12 18 47.8 | +47 20 51.7 | 828, 470, 444 | 7.0, 2.8, 2.8 | ... | sa | |
| NGC 4258 XMM2 | 12 18 57.8 | +47 16 06.8 | 732, 337, 337 | 5.8, 2, 2.1 | NGC 4258 [RW2000] X-7 | sa | |
| | ... | ... | 716, 268, 290 | 1.8, 1, 1.0 | ... | ... | |
| NGC 4258 XMM3 | 12 18 56.5 | +47 21 24.3 | 489, 182, 184 | 3.8, 0.9, 1.1 | NGC 4258 [RW2000] X-5 | sa | |
| | ... | ... | ..., 160, 142 | ..., 0.3, 0.3 | ... | ... | |
| NGC 4258 XMM4 | 12 19 23.2 | +47 09 37.2 | 644, 277, 224 | 4.9, 1.3, 1.3 | HELLAS 288 | Edge sa? | |
| | ... | ... | 964, 410, 382 | 0.3, 0.2, 0.1 | ... | ... | |
| NGC 4395 XMM1 | 12 26 01.5 | +33 31 29 | 2162, 862, 921 | 15.5, 5.1, 5.6 | NGC 4395 [RW2000] X-1; IXO 53 | sa | |
| NGC 4395 XMM2 | 12 25 25.3 | +33 36 46.4 | 392, 252, 208 | 2.6, 1.5, 1.2 | ... | sa? | |
| NGC 4395 XMM3 | 12 25 32.6 | +33 25 27.9 | 763, 277, 278 | 5.2, 1.5, 1.6 | ... | Out? | |
| NGC 4395 XMM4 | 12 25 42.7 | +33 40 00.1 | 516, 60, 40 | 3.1, 0.3, 0.2 | ... | Out | |
| NGC 4449 XMM1 | 12 28 18 | +44 06 30.9 | 1409, 608, 593 | 10.6, 3.6, 3.5 | XRB?; NGC 4449 [RW2000] X-7; source 27 ^m | sa | |
| NGC 4449 XMM2 | 12 28 09.3 | +44 05 03.9 | 1503, 527, 586 | 11.3, 3.1, 3.5 | SNR?; NGC 4449 [RW2000] X-1; source 10 | sa | |
| NGC 4449 XMM3 | 12 28 11.1 | +44 06 43.9 | 1094, 549, 404 | 8.3, 3.2, 2.3 | SNR; source 15 | sa | |
| NGC 4490 XMM1 | 12 30 32.4 | +41 39 14.6 | 746, 323, 393 | 6.0, 1.9, 2.2 | NGC 4490 [RW2000] X-1 | sa | |
| NGC 4490 XMM2 | 12 30 36.5 | +41 38 33.3 | 656, 299, 310 | 5.3, 1.7, 1.7 | NGC 4490 [RW2000] X-2 | Near center | |
| NGC 4490 XMM3 | 12 30 43.3 | +41 38 11.5 | 832, 501, 461 | 5.8, 2.6, 2.2 | NGC 4490 [RW2000] X-4 | sa | |
| NGC 4490 XMM4 | 12 30 31.1 | +41 39 08.1 | 546, 291, 286 | 4.4, 1.7, 1.6 | CXOU J123030.8 +413911 | sa | |
| NGC 4490 XMM5 | 12 30 30.3 | +41 41 40.3 | 413, 587, 482 | 2.7, 3.1, 2.3 | NGC 4485 [RW2000] X-1 | sa | |
| NGC 4631 XMM1 | 12 41 55.8 | +32 32 14 | 5093, 1969, 1762 | 13, 4.2, 3.8 | NGC 4631 [RW2000] X-1; IXO 68 | sa | |
| NGC 4631 XMM2 | 12 41 57.5 | +32 32 01 | 1273, 531, 400 | 3.3, 1.2, 0.9 | NGC 4631 [RW2000] X-2 | sa | |
| NGC 4631 XMM3 | 12 41 58.2 | +32 28 49.6 | 1271, 443, 457 | 2.8, 0.9, 0.9 | CXOUSEXSI J124158.0+322851 | Out | |
| NGC 4631 XMM4 | 12 42 16.1 | +32 32 48.8 | 957, 400, 429 | 2.3, 0.8, 0.8 | [VP96] H13 | sa | |
| NGC 4631 XMM5 | 12 42 11.2 | +32 32 33.6 | 1626, 894, 866 | 3.9, 1.9, 1.8 | [VP96] H12; [HFE2003] PSX-01 | sa | |
| NGC 4736 XMM1 | 12 50 50.2 | +41 07 12 | 713, 273, 227 | 6.7, 2.1, 1.7 | NGC 4736 X-4 ⁿ | Near center | |
| NGC 4945 XMM1 | 13 05 33.3 | -49 27 36.3 | 1456, 646, 595 | 7.9, 2.9, 2.6 | NGC 4945 [GMB2000] X-2 | sa | |
| NGC 4945 XMM2 | 13 05 38.4 | -49 25 45.3 | 1393, 600, 523 | 7.6, 2.7, 2.3 | NGC 4945 [R97] X-3 | sa | |
| NGC 4945 XMM3 | 13 05 18.8 | -49 28 24 | ..., 357, 362 | ..., 1.6, 1.6 | ... | sa | |
| NGC 4945 XMM4 | 13 05 22.2 | -49 28 26.3 | 731, 331, 332 | 4.0, 1.5, 1.5 | NGC 4945 [BIR96] X-1? | sa | |
| NGC 4945 XMM5 | 13 05 25.7 | -49 28 30.7 | 772, 267, 301 | 4.2, 1.2, 1.32 | ... | sa | |
| NGC 5204 XMM1 | 13 29 38.5 | +58 25 03.6 | 9981, 3352, 3384 | 62.8, 17.7, 17.9 | NGC 5204 [RW2000] X-1; IXO 77 | sa | 11 |
| | ... | ... | 9231, 2284, 2349 | 85.5, 24.7, 25.8 | ... | ... | |
| NGC 5204 XMM2 | 13 29 27.4 | +58 25 31.8 | 573, 170, 231 | 3.4, 0.8, 1.2 | ... | Edge sa | |
| | ... | ... | 772, 161, 121 | 5.0, 1.7, 1.1 | ... | ... | |
| M51 XMM1..... | 13 29 40 | +47 12 36.2 | 1102, 367, 409 | 6.2, 1.8, 2 | NGC 5194 [RW2000] X-1 | sa | |
| M51 XMM2..... | 13 30 07.7 | +47 11 04.8 | 514, 540, 549 | 2.6, 2.2, 2.2 | IXO 81 | sa | |
| M51 XMM3..... | 13 30 01.1 | +47 13 41.4 | 1004, 315, 311 | 4.1, 1.1, 1.1 | CXOU J133001.0 +471344; IXO 80 | sa | |
| M51 XMM4..... | 13 30 06 | +47 15 38.9 | 518, 183, 166 | 2.8, 0.9, 0.8 | NGC 5195 [RW2000] X-1 | sa | |
| M51 XMM5..... | 13 29 59.6 | +47 15 54 | 1079, 359, 257 | 5, 1.5, 1 | CXOU J132959.5 +471559 | Near center | |
| M51 XMM6..... | 13 29 57.5 | +47 10 45.3 | 536, 206, 247 | 1.9, 0.6, 0.8 | CXOU J132957.6 +471048 | sa | |
| M51 XMM7..... | 13 29 53.6 | +47 14 31.5 | 452, 141, 143 | 2.4, 0.6, 0.7 | CXOU J132953.8 +471432 | Edge sa | |
| M83 XMM1..... | 13 37 19.8 | -29 53 49.8 | 3074, 927, 987 | 12, 3.3, 2.5 | RX J133719 -2953.6; IXO 82 | sa | |
| M83 XMM2..... | 13 36 59.4 | -29 49 57.2 | 1133, 371, 397 | 4, 1.3, 1 | CXOU J133659.4 -294959 | sa | |
| M83 XMM3 ^o | 13 37 04.4 | -29 51 24 | 1724, 576, 459 | 7.2, 2.3, 1.2 | CXOU J133704.3 -295121 | sa | |

TABLE 6—Continued

| Source ^a | R.A. | Decl. | Total Counts | Count Rate ^b (10 ⁻² counts s ⁻¹) | ID | Location in Galaxy ^c | <i>XMM-Newton</i> References ^d |
|----------------------------------|------------|-------------|-------------------|---|---|------------------------------------|--|
| M83 XMM4..... | 13 37 01.5 | -29 53 26 | 1289, 345, 401 | 4.9, 1.3, 1.0 | CXOU J133701.4 -295326 | sa | |
| NGC 5253 ^p | ... | ... | ... | ... | ... | ... | ... |
| M101 XMM1..... | 14 03 14.7 | +54 18 05 | 2690, 1449, 1417 | 10.3, 3.3, 3.3 | CXOU J140313.9 +541811; XMM2 ^q | sa | 12 |
| M101 XMM2..... | 14 03 03.8 | +54 27 37 | 2825, 1623, 1551 | 10.3, 3.6, 3.3 | XMM1 | Edge sa? | 12 |
| M101 XMM3..... | 14 04 14.6 | +54 26 04.4 | 1460, 822, 717 | 5, 1.6, 1.3 | CXOU J140414.3 +542604; XMM3 | Edge sa? | 12 |
| M101 XMM4..... | 14 02 28.5 | +54 16 26.7 | 1505, 877, 757 | 5.1, 1.7, 1.5 | CXOU J140228.3 +541626 | sa | 12 |
| M101 XMM5..... | 14 02 22.5 | +54 17 58 | 516, 245, 289 | 1.8, 0.4, 0.6 | CXOU J140222.2 +541756; XMM6 | sa | 12 |
| NGC 5408 XMM1..... | 14 03 19.8 | -41 22 59.3 | 5932, 2036, 2077 | 12.8, 3.2, 3.3 | NGC 5408 [KCP2003] X-1 | sa | 5 |
| Circinus XMM1 ^r | 14 12 54.2 | -65 22 55.3 | 16220, 11452, ... | 14.5, 11.3, ... | ... | Edge sa? | |
| Circinus XMM2..... | 14 12 39.2 | -65 23 34.3 | 8741, 2386, ... | 5.7, 1.9, ... | ... | Edge sa? | |
| Circinus XMM3..... | 14 13 28.3 | -65 18 08.3 | 4873, 1031, ... | 1.8, 0.7, ... | ... | Edge sa? | |

NOTES.—Units of right ascension are hours, minutes, and seconds, and units of declination are degrees, arcminutes, and arcseconds. Table 6 is also available in machine-readable form in the electronic edition of the *Astrophysical Journal*.

^a Sources labeled XMM*N* in order of apparent brightness from the first observation studied.

^b Count rate for the PN, MOS1, and MOS2 spectra.

^c Location specified as follows: inside the optical extent of the galaxy or in spiral arms (sa), near the center of the galaxy, at the edge of a spiral arm/optical extent of galaxy, or outside the optical extent of the galaxy. Location based on DSS images.

^d References to studies using *XMM-Newton* spectra.

^e Identification for NGC 0253 following Humphrey et al. (2003).

^f Transient.

^g Appears as an extended source in the *HST* image.

^h Spectra too scattered to model.

ⁱ Bright sources coincide with nucleus (unresolvable star cluster and X-ray binaries), foreground star, and background AGN (Martin et al. 2002).

^j IXO designation from Colbert & Ptak (2002).

^k Spectrum from Hol IX observation.

^l Bright source is too close to other sources.

^m *Chandra* observations of point sources in NGC 4449 published in Summers et al. (2003); source 27 varied from *ROSAT* observations.

ⁿ Three other sources near the nucleus are unresolvable in the *XMM-Newton* observations but seen by *Chandra* (Eracleous et al. 2002).

^o Unable to model the spectrum due to an error in χ^2 space.

^p Bright sources are too close but resolvable by *Chandra* (Summers et al. 2004).

^q Alternate ID from Jenkins et al. (2004).

^r Bright sources near the nucleus are unresolvable but seen by *Chandra* (Smith & Wilson 2001).

REFERENCES.—(1) Pietsch et al. 2001; (2) Pietsch et al. 2003; (3) Kong & Di Stefano 2003; (4) Miller et al. 2004; (5) Wang et al. 2004; (6) Schlegel et al. 2004; (7) Bauer et al. 2003; (8) Kong 2003; (9) Lehmann et al. 2005; (10) Zimmermann & Aschenbach 2003; (11) Roberts et al. 2005; (12) Jenkins et al. 2004.

TABLE 7
BRIGHT, IDENTIFIABLE BACKGROUND AND FOREGROUND SOURCES

| Galaxy | R.A. | Decl. | Identification |
|-----------------------------|------------|-------------|--|
| NGC 247..... | 00 46 51.7 | -20 43 30 | QSO B044-2059 |
| NGC 300..... | 00 55 26.7 | -37 31 25.6 | HD 5403 (star) |
| NGC 625..... | 01 34 42.4 | -41 36 15.2 | QSO B0132-4151 |
| NGC 1569 ^a | 04 31 16.9 | +64 49 50 | CXOU J043116.8+644950 (star) |
| NGC 1569..... | 04 31 14.2 | +64 51 07.9 | CXOU 043114.0+645107 (star) |
| NGC 1569..... | 04 31 25.4 | +64 51 53.8 | CXOU 043125.1+645154 (AGN) |
| NGC 1705..... | 04 54 01.2 | -53 21 12.3 | WGA J0454.0-5320 (M star or elliptical galaxy) |
| NGC 2403..... | 07 35 09 | +65 40 27.5 | HD 59581 (star) |
| NGC 4258..... | 12 18 08.9 | +47 16 08.3 | QSO J1218+472 |
| M83..... | 13 36 45.6 | -29 59 13.9 | 2MASX J13364579-2959122 (galaxy) |
| M83..... | 13 36 13.9 | -29 56 13 | RX J133615-2957.8 (galaxy) |
| NGC 5253..... | 13 39 50.6 | -31 34 11.1 | CD -30 10790 (star) |
| M101..... | 14 02 30 | +54 21 18.2 | [WIP99] H13 (star) ^b |
| NGC 5408..... | 14 03 27.5 | -41 25 18.5 | (Star) |

NOTE.—Units of right ascension are hours, minutes, and seconds, and units of declination are degrees, arcminutes, and arcseconds.

^a Identification for objects in NGC 1569 from Martin et al. (2002).

^b Confirmed by K. Kuntz using *HST* ACS.

TABLE 8
XMM-Newton POWER-LAW FIT FOR BEST-FIT TWO-COMPONENT SPECTRA

| Source | n_{H}^{a} (10^{21} cm^{-2}) | Γ | χ^2/dof | F_{X}^{b} ($10^{-12} \text{ ergs cm}^{-2} \text{ s}^{-1}$) | L_{X}^{c} ($10^{39} \text{ ergs s}^{-1}$) |
|----------------------------|--|--|---------------------|---|--|
| NGC 247 XMM1 | 9.5 ^{+1.6} _{-1.4} | 8.52 ^{+1.14} _{-0.91} | 112.2/95 | 1900 | 2200 |
| NGC 253 XMM1 | 3.4 ^{+0.3} _{-0.3} | 1.77 ^{+0.06} _{-0.06} | 262.6/232 | 3.1 | 3.6 |
| NGC 253 XMM2 (obs 2)..... | 6.9 ^{+0.4} _{-0.4} | 1.98 ^{+0.05} _{-0.05} | 611.6/582 | 2.9 | 3.3 |
| NGC 253 XMM3 | 2.2 ^{+0.1} _{-0.1} | 2.03 ^{+0.04} _{-0.04} | 507.4/500 | 1.2 | 1.4 |
| NGC 253 XMM4 | 3.9 ^{+0.5} _{-0.4} | 2.17 ^{+0.14} _{-0.11} | 91.9/83 | 0.73 | 1.2 |
| NGC 253 XMM5 | 4.0 ^{+0.4} _{-0.3} | 2.06 ^{+0.09} _{-0.07} | 381.8/409 | 0.98 | 1.6 |
| NGC 253 XMM6 | 8.5 ^{+3.0} _{-2.3} | 2.09 ^{+0.33} _{-0.28} | 73.6/59 | 0.52 | 0.85 |
| NGC 253 XMM7 | 1.2 ^{+0.3} _{-0.15} | 2.09 ^{+0.16} _{-0.15} | 321.4/293 | 0.29 | 0.48 |
| NGC 300 XMM1 | 1.7 ^{+1.2} _{-0.9} | 1.54 ^{+0.22} _{-0.20} | 31.8/25 | 0.32 | 0.53 |
| NGC 300 XMM2 | 3.4 ^{+0.2} _{-0.2} | 2.17 ^{+0.7} _{-0.7} | 283.8/298 | 1.1 | 1.3 |
| NGC 300 XMM3 | 3.9 ^{+0.3} _{-0.3} | 2.21 ^{+0.84} _{-0.80} | 435/409 | 0.93 | 1.5 |
| NGC 300 XMM5 | 7.1 ^{+0.7} _{-0.7} | 2.15 ^{+0.11} _{-0.11} | 357/342 | 1.3 | 2.2 |
| NGC 300 XMM6 | 0.97 ^{+0.11} _{-0.11} | 2.67 ^{+0.06} _{-0.06} | 469.8/422 | 0.81 | 0.6 |
| NGC 300 XMM7 | 1.7 ^{+0.40} _{-0.40} | 3.20 ^{+0.32} _{-0.24} | 133.98/99 | 0.27 | 0.21 |
| NGC 300 XMM8 | 3.4 ^{+0.8} _{-0.6} | 1.86 ^{+0.15} _{-0.13} | 101.9/81 | 0.19 | 0.15 |
| NGC 300 XMM9 | 0.311 ^d | 2.29 ^{+0.15} _{-0.14} | 54.2/56 | 0.14 | 0.10 |
| NGC 300 XMM10 | ? | 2.05 ^{+0.17} _{-0.15} | 47.6/37 | 0.06 | 0.15 |
| NGC 1313 XMM1 | 1.5 ^{+0.2} _{-0.2} | 1.81 ^{+0.08} _{-0.09} | 219.8/203 | 0.42 | 0.88 |
| NGC 1313 XMM2 | 2.8 ^{+0.16} _{-0.16} | 2.48 ^{+0.07} _{-0.06} | 464.1/421 | 1.9 | 4.0 |
| NGC 1313 XMM3 | 3.6 ^{+0.2} _{-0.2} | 3.2 ^{+0.09} _{-0.09} | 778.3/426 | 3.3 | 6.9 |
| IC 0342 XMM3..... | 3.8 ^{+0.4} _{-0.4} | 2.58 ^{+0.15} _{-0.14} | 185.8/109 | 1.7 | 3.1 |
| NGC 1705 XMM1 | 0.3 ^d | 1.93 ^{+0.11} _{-0.10} | 61.9/88 | 0.12 | 0.37 |
| NGC 1705 XMM2 | 1.4 ^{+0.45} _{-0.41} | 2.12 ^{+0.26} _{-0.15} | 91/76 | 0.078 | 0.24 |
| NGC 1705 XMM3 | 0.6 ^{+0.36} _{-0.40} | 1.36 ^{+0.12} _{-0.13} | 80.9/67 | 0.17 | 0.53 |
| NGC 2403 XMM1 | 3.2 ^{+0.61} _{-0.55} | 2.15 ^{+0.16} _{-0.15} | 92.2/81 | 2.2 | 3.6 |
| NGC 2403 XMM2 | 2.7 ^{+0.37} _{-0.34} | 2.07 ^{+0.11} _{-0.11} | 179.5/151 | 1.3 | 2.0 |
| NGC 2403 XMM3 | 1.9 ^{+0.40} _{-0.36} | 1.97 ^{+0.14} _{-0.13} | 92.6/107 | 0.81 | 1.3 |
| Holm II XMM1 (obs 1) | 1.5 ^{+0.07} _{-0.07} | 2.61 ^{+0.04} _{-0.04} | 1134.2/976 | 12 | 10 |
| Holm I XMM1..... | ? | 2.04 ^{+0.14} _{-0.07} | 102.8/95 | 0.48 | 1.7 |
| M81 XMM1..... | 3.2 ^{+0.07} _{-0.07} | 2.09 ^{+0.02} _{-0.02} | 1849.9/1245 | 4.5 | 7.0 |
| M81 XMM2..... | 3.0 ^{+0.3} _{-0.3} | 1.79 ^{+0.07} _{-0.07} | 224.9/208 | 4.3 | 6.7 |
| M81 XMM3..... | 7.3 | 6.13 | 1358.2/618 | 48.5 | 75.2 |
| M81 XMM4..... | 0.97 ^{+0.25} _{-0.41} | 1.58 ^{+0.18} _{-0.15} | 81.35/80 | 2.5 | 3.9 |
| M81 XMM5..... | ? | 0.88 ^{+0.11} _{-0.11} | 66.4/52 | 0.35 | 0.54 |
| M81 XMM6..... | 1.0 ^{+0.4} _{-0.3} | 1.52 ^{+0.11} _{-0.11} | 97.5/82 | 0.44 | 0.68 |
| Holm IX XMM1..... | 1.7 ^{+0.08} _{-0.08} | 1.84 ^{+0.03} _{-0.03} | 1000.9/882 | 9.4 | 15 |
| Sextans A XMM1..... | 0.18 ^{+0.23} _{-0.16} | 2.25 ^{+0.12} _{-0.07} | 271.4/275 | 0.56 | 0.13 |
| NGC 4214 XMM2 | 0.2 ^{+0.5} _{-0.2} | 2.03 ^{+0.43} _{-0.28} | 50.9/46 | 0.16 | 0.14 |
| NGC 4258 XMM1 | 1.6 ^{+0.4} _{-0.4} | 1.9 ^{+0.14} _{-0.13} | 101.4/78 | 0.06 | 0.04 |
| NGC 4258 XMM2 (obs 1)..... | 3.5 ^{+0.9} _{-0.7} | 1.88 ^{+0.16} _{-0.15} | 97.5/63 | 0.43 | 2.6 |
| NGC 4395 XMM1 | 3.7 ^{+0.5} _{-0.4} | 4.93 ^{+0.34} _{-0.30} | 195.1/156 | 7.2 | 14 |
| NGC 4395 XMM2 | ? | 1.86 ^{+0.14} _{-0.09} | 55.9/58 | 0.25 | 0.48 |
| NGC 4449 XMM1 | 6.3 ^{+0.9} _{-0.7} | 2.22 ^{+0.14} _{-0.12} | 103/118 | 1.2 | 1.36 |
| NGC 4449 XMM2 | 3.3 ^{+0.5} _{-0.4} | 3.36 ^{+0.29} _{-0.23} | 154/89 | 1.3 | 1.5 |
| NGC 4490 XMM1 | 0.83 ^{+0.14} _{-0.12} | 2.53 ^{+0.17} _{-0.16} | 101.5/65 | 1.2 | 8.7 |
| NGC 4490 XMM2 | 6.3 ^{+1.3} _{-1.0} | 2.36 ^{+0.19} _{-0.17} | 49.5/56 | 0.92 | 6.7 |
| NGC 4490 XMM3 | 9.4 ^{+1.5} _{-1.2} | 2.95 ^{+0.24} _{-0.20} | 76.7/80 | 1.5 | 11 |
| NGC 4631 XMM1 | 2.3 ^{+0.16} _{-0.15} | 2.13 ^{+0.06} _{-0.05} | 383.4/347 | 0.76 | 5.1 |
| NGC 4631 XMM2 | 1.9 ^{+0.4} _{-0.3} | 2.01 ^{+0.14} _{-0.12} | 119.5/99 | 0.23 | 1.5 |
| NGC 4631 XMM3 | 0.63 ^{+0.3} _{-0.2} | 1.53 ^{+0.1} _{-0.08} | 146/98 | 0.15 | 1.0 |
| NGC 4736 XMM1 | 0.95 ^{+0.6} _{-0.5} | 2.02 ^{+0.26} _{-0.25} | 62.8/53 | 0.36 | 0.80 |
| NGC 4945 XMM1 | 5.8 ^{+0.8} _{-0.7} | 1.88 ^{+0.08} _{-0.10} | 116/122 | 0.9 | 1.0 |
| NGC 4945 XMM2 | 3.4 ^{+0.6} _{-0.5} | 1.58 ^{+0.09} _{-0.10} | 114.5/115 | 0.71 | 0.82 |
| NGC 4945 XMM3 | 5.2 ^{+0.8} _{-0.7} | 2.59 ^{+0.19} _{-0.17} | 75.5/62 | 0.49 | 0.56 |
| NGC 5204 XMM1 | 0.61 ^{+0.1} _{-0.1} | 2.11 ^{+0.04} _{-0.04} | 592.1/561 | 2.0 | 5.5 |
| M51 XMM1..... | 1.1 ^{+0.1} _{-0.1} | 2.41 ^{+0.07} _{-0.07} | 533/498 | 3.0 | 8.3 |
| M51 XMM2..... | 1.1 ^{+0.30} _{-0.27} | 2.67 ^{+0.20} _{-0.16} | 110.5/82 | 0.34 | 2.8 |
| M51 XMM3..... | 2.3 ^{+0.50} _{-0.30} | 2.50 ^{+0.22} _{-0.20} | 75.2/70 | 0.52 | 3.3 |
| M51 XMM4..... | 2.7 | 3.08 | 256.0/72 | 0.43 | 2.7 |
| M51 XMM5..... | 2.0 ^{+0.83} _{-0.72} | 2.50 ^{+0.33} _{-0.25} | 40.97/43 | 0.13 | 0.83 |
| M51 XMM6..... | 0.5 ^{+0.39} _{-0.46} | 1.95 ^{+0.23} _{-0.18} | 37.8/31 | 0.11 | 0.66 |
| M83 XMM1..... | 1.9 ^{+0.34} _{-0.31} | 2.32 ^{+0.13} _{-0.12} | 210.9/211 | 0.64 | 2.8 |
| M83 XMM2..... | 6.0 ^{+1.8} _{-1.3} | 2.54 ^{+0.26} _{-0.23} | 91.4/91 | 0.4 | 1.8 |
| M101 XMM1..... | 0.56 ^{+0.15} _{-0.14} | 1.98 ^{+0.08} _{-0.08} | 303/233 | 0.45 | 2.9 |
| M101 XMM2..... | 2.2 ^{+0.25} _{-0.23} | 1.85 ^{+0.07} _{-0.07} | 288.8/263 | 0.81 | 5.3 |
| M101 XMM3..... | 1.5 ^{+0.4} _{-0.3} | 2.70 ^{+0.21} _{-0.17} | 148.9/133 | 0.51 | 3.4 |
| M101 XMM4..... | 2.2 ^{+0.45} _{-0.42} | 2.25 ^{+0.20} _{-0.17} | 165.7/140 | 0.38 | 2.5 |

TABLE 8—Continued

| Source | n_{H}^{a} (10^{21} cm^{-2}) | Γ | χ^2/dof | F_{X}^{b} ($10^{-12} \text{ ergs cm}^{-2} \text{ s}^{-1}$) | L_{X}^{c} ($10^{39} \text{ ergs s}^{-1}$) |
|---------------------|--|------------------------|---------------------|---|--|
| M101 XMM5..... | $1.3^{+0.2}_{-0.3}$ | $2.28^{+0.12}_{-0.11}$ | 47.9/46 | 0.12 | 0.8 |
| NGC 5408 XMM1 | $1.6^{+0.2}_{-0.1}$ | $3.57^{+0.12}_{-0.11}$ | 396.8/339 | 7.04 | 19.4 |
| Circinus XMM1 | $7.6^{+0.3}_{-0.3}$ | $2.15^{+0.05}_{-0.04}$ | 762.9/863 | 4.6 | 8.8 |
| Circinus XMM2..... | $11.7^{+0.4}_{-0.7}$ | $3.48^{+0.13}_{-0.06}$ | 517.9/432 | 2.7 | 5.2 |
| Circinus XMM3..... | $9.0^{+2.1}_{-1.0}$ | $2.57^{+0.40}_{-0.17}$ | 285.2/262 | 0.32 | 0.61 |

^a Total column density.

^b Unabsorbed flux in the 0.3–10 keV band.

^c Unabsorbed luminosity in the 0.3–10 keV band, using the distances quoted in Table 1.

^d Absorption level frozen at Galactic level.

TABLE 9
BEST-FIT ABSORBED COMPTONIZATION MODEL PARAMETERS

| ID | n_{H}^{a} (10^{21} cm^{-2}) | kT^{b} (keV) | τ^{c} | χ^2 | F_{X}^{d} ($10^{-12} \text{ ergs cm}^{-2} \text{ s}^{-1}$) |
|---------------------|--|--------------------------|-----------------------|-----------|---|
| NGC 253 XMM2 | $1.8^{+0.08}_{-0.16}$ | $1.28^{+0.13}_{-0.12}$ | $19.59^{+2.0}_{-1.6}$ | 464/498 | 1.47 |
| NGC 2403 XMM1 | $1.95^{+1.2}_{-0.6}$ | $0.98^{+0.16}_{-0.15}$ | $25.4^{+7.2}_{-8.3}$ | 82.8/85 | 1.4 |
| NGC 4490 XMM1 | $4.7^{+1.1}_{-2.1}$ | $0.96^{+0.13}_{-0.16}$ | $27.0^{+18.3}_{-4.9}$ | 66.5/64 | 0.66 |
| NGC 4490 XMM2 | $5.0^{+1.6}_{-1.4}$ | $1.21^{+0.21}_{-0.31}$ | $18.8^{+8.6}_{-9.7}$ | 45.7/55 | 0.67 |
| M101 XMM2..... | $1.6^{+0.26}_{-0.24}$ | $1.24^{+0.09}_{-0.15}$ | $23.3^{+3.4}_{-2.8}$ | 256/262 | 0.65 |
| M101 XMM3..... | $1.1^{+0.43}_{-0.40}$ | 1.13 | 15.2 | 128/132 | 0.41 |
| Circinus XMM2..... | $6.8^{+1.3}_{-0.9}$ | $0.62^{+0.08}_{-0.04}$ | $29.7^{+8.1}_{-7.0}$ | 437.2/430 | 0.5 |
| Circinus XMM3..... | $6.7^{+1.6}_{-2.4}$ | $0.93^{+0.28}_{-0.24}$ | $23.1^{+17.5}_{-5.2}$ | 273.1/261 | 0.17 |

^a Total column density.

^b Temperature.

^c Optical depth.

^d Unabsorbed flux in the 0.3–10 keV band.

TABLE 10
XMM-Newton GALAXY OBSERVATIONS: INFRARED DETAILS AND NUMBER OF ULXs

| Galaxy | S_{60} (Jy) | S_{100} (Jy) | F_{FIR} ($10^{-9} \text{ ergs cm}^{-2} \text{ s}^{-1}$) | L_{FIR} ($10^{42} \text{ ergs s}^{-1}$) | Number of ULXs |
|------------------|------------------|-------------------|---|---|----------------|
| NGC 247..... | 7.93 | 27.32 | 0.602 | 0.687 | 1 |
| NGC 253..... | 998.73 | 1861.67 | 55.92 | 93.10 | 3 |
| NGC 300..... | 23.08 | 74.45 | 1.688 | 1.324 | 0 |
| NGC 625..... | 5.09 | 9.08 | 0.280 | 0.230 | 0 |
| NGC 1313..... | 35.97 | 92.00 | 2.329 | 4.845 | 2 |
| IC 0342..... | 255.96 | 661.68 | 16.66 | 30.32 | 3 |
| NGC 1569..... | 45.41 | 47.29 | 2.072 | 0.635 | 0 |
| NGC 1705..... | 0.970 | 2.580 | 0.064 | 0.199 | 0 |
| Mrk 71..... | 3.51 | 4.67 | 0.173 | 0.239 | 1 |
| NGC 2403..... | 51.55 | 148.49 | 3.547 | 5.378 | 2 |
| Holmberg II..... | 1.15 | 2.62 | 0.070 | 0.061 | 1 |
| Holmberg I..... | ... | ... | ... | ... | 1 |
| M81..... | 44.73 | 174.02 | 3.647 | 5.655 | 1 |
| M82..... | 1271.32 | 1351.09 | 58.35 | 106.2 | 1 |
| Holmberg IX..... | ... | ... | ... | ... | 1 |
| Sextans A..... | 0.255 | 0.674 | 0.017 | 0.004 | 0 |
| IC 2574..... | 2.41 | 10.62 | 0.212 | 0.329 | 0 |
| NGC 4214..... | 17.87 | 29.04 | 0.947 | 0.826 | 1 |
| NGC 4258..... | 21.60 | 78.39 | 1.690 | 10.48 | 1 |
| NGC 4395..... | 4.21 | 12.90 | 0.299 | 0.573 | 1 |
| NGC 4449..... | 37.00 | 58.28 | 1.937 | 2.199 | 1 |
| NGC 4490..... | 47.79 | 85.94 | 2.636 | 19.19 | 5 |
| NGC 4631..... | 82.90 | 208.66 | 5.324 | 35.83 | 1 |
| NGC 4736..... | 62.41 | 135.34 | 3.734 | 8.261 | 4 |
| NGC 4945..... | 588.11 | 1415.5 | 36.95 | 42.49 | 0 |
| NGC 5204..... | 2.33 | 5.35 | 0.143 | 0.395 | 2 |
| M51..... | 108.68 | 292.08 | 7.213 | 44.74 | 5 |
| M83..... | 266.03 | 638.63 | 16.69 | 76.79 | 0 |
| NGC 5253..... | 30.00 | 30.92 | 1.365 | 16.72 | 0 |
| M101..... | 88.04 | 252.84 | 6.048 | 39.63 | 4 |
| NGC 5408..... | 2.825 | 2.958 | 0.129 | 0.356 | 1 |
| Circinus..... | 248.7 | 315.85 | 12.06 | 23.10 | 4 |

REFERENCES

- Anderson, S., et al. 2003, *AJ*, 126, 2209
- Bauer, F. E., Brandt, W. N., & Lehmer, B. 2003, *AJ*, 126, 2797
- Begelman, M. C. 2002, *ApJ*, 568, L97
- Belloni, T., et al. 1997, *ApJ*, 488, L109
- Chen, W., Schrader, C. R., & Livio, M. 1997, *ApJ*, 491, 312
- Colbert, E. J. M., & Ptak, A. F. 2002, *ApJS*, 143, 25
- Done, C., & Gierliński, M. 2003, *MNRAS*, 342, 1041
- Ebisawa, K., et al. 2003, *ApJ*, 597, 780
- Eracleous, M., Shields, J. C., Chartas, G., & Moran, E. C. 2002, *ApJ*, 565, 108
- Freedman, W. L., et al. 1994, *ApJ*, 427, 628
- Freeman, K. C., Karlsson, B., Lynga, G., Burrell, J. F., van Woerden, H., & Goss, W. M. 1977, *A&A*, 55, 445
- Gierliński, M., & Done, C. 2004, *MNRAS*, 349, L7
- Grimm, H.-J., Gilfanov, M., & Sunyaev, R. 2003, *MNRAS*, 339, 793
- Gültekin, K., Miller, M. C., & Hamilton, D. P. 2004, *ApJ*, 616, 221
- Gutiérrez, C. M., & López-Corredoira, M. 2005, *ApJ*, 622, L89
- Heger, A., & Woosley, S. E. 2002, *ApJ*, 567, 532
- Ho, L. C., Filippenko, A. V., & Sargent, W. L. W. 1997, *ApJS*, 112, 315
- Humphrey, P. J., Fabbiano, G., Elvis, M., Church, M. J., & Balucinska-Church, M. 2003, *MNRAS*, 344, 134
- Jenkins, L. P., Roberts, T. P., Warwick, R. S., Kilgard, R. E., & Ward, M. J. 2004, *MNRAS*, 349, 404
- Jones, C. 1977, *ApJ*, 214, 856
- Jonker, P. G., & Nelemans, G. 2004, *MNRAS*, 354, 355
- Kalogera, V., Henninger, M., Ivanova, N., & King, A. R. 2004, *ApJ*, 603, L41
- Karachentsev, I. D., et al. 2002, *A&A*, 385, 21
- Kelson, D. D. 1996, *ApJ*, 463, 26
- King, A. R., et al. 2001, *ApJ*, 552, L109
- Kong, A. K. H. 2003, *MNRAS*, 346, 265
- Kong, A. K. H., & Di Stefano, R. 2003, *ApJ*, 590, L13
- Kording, E., Falcke, H., & Markoff, S. 2002, *A&A*, 382, L13
- Kubota, A., & Makishima, K. 2004, *ApJ*, 601, 428
- Kubota, A., et al. 2001, *ApJ*, 560, L147
- Kuntz, K., et al. 2005, *ApJ*, 620, L31
- Lehmann, I., et al. 2005, *A&A*, 431, 847
- Liu, J. F., Bregman, J. N., & Seitzer, P. 2004, *ApJ*, 602, 249
- Madau, P., & Rees, M. J. 2001, *ApJ*, 551, L27
- Magdziarz, P., & Zdziarski, A. A. 1995, *MNRAS*, 273, 837
- Makishima, K., et al. 2000, *ApJ*, 535, 632
- Martin, C. L., Kobulnicky, H. A., & Heckman, T. M. 2002, *ApJ*, 574, 663
- Miller, J. M., Fabbiano, G., Miller, M. C., & Fabian, A. C. 2003, *ApJ*, 585, L37
- Miller, J. M., Fabian, A. C., & Miller, M. C. 2004, *ApJ*, 614, L117
- Miller, M. C., & Colbert, E. J. M. 2004, *Int. J. Mod. Phys. D*, 13, 1
- Miller, M. C., & Hamilton, D. P. 2002, *MNRAS*, 330, 232
- Miyamoto, S., et al. 1991, *ApJ*, 383, 784
- Pakull, M. W., & Mirioni, L. 2003, *Rev. Mex. AA Ser. Conf.*, 15, 197
- Pietsch, W., Haberl, F., & Vogler, A. 2003, *A&A*, 402, 457
- Pietsch, W., et al. 2001, *A&A*, 365, L174
- Porquet, D., Reeves, J. N., O'Brien, P., & Brinkmann, W. 2004, *A&A*, 422, 85
- Ptak, A., & Colbert, E. 2004, *ApJ*, 606, 291
- Ranalli, P., Comastri, A., & Setti, G. 2003, *A&A*, 399, 39
- Remillard, R. A., & McClintock, J. E. 2006, *ARA&A*, in press (astro-ph/0606352)
- Reynolds, C. S., et al. 1997, *MNRAS*, 286, 349
- Roberts, T. P., Warwick, R. S., Ward, M. J., & Goad, M. R. 2004, *MNRAS*, 349, 1193
- Roberts, T. P., et al. 2005, *MNRAS*, 357, 1363
- Ross, R. R., & Fabian, A. C. 2005, *MNRAS*, 358, 211
- Sakai, S., & Madore, B. F. 1999, *ApJ*, 526, 599
- Sakai, S., Madore, B. F., & Freedman, W. L. 1996, *ApJ*, 461, 713
- Schlegel, E. M., et al. 2004, *ApJ*, 603, 644
- Shapley, A., Fabbiano, G., & Eskridge, P. B. 2001, *ApJS*, 137, 139
- Smith, D. A., & Wilson, A. S. 2001, *ApJ*, 557, 180
- Stocke, J. T., et al. 1983, *ApJ*, 273, 458
- Summers, L. K., Stevens, I. R., Strickland, D. K., & Heckman, T. M. 2003, *MNRAS*, 342, 690
- . 2004, *MNRAS*, 351, 1
- Sunyaev, R. A., & Titarchuk, L. G. 1980, *A&A*, 86, 121
- Swartz, D. A., Ghosh, K. K., Tennant, A. F., & Wu, K. 2004, *ApJS*, 154, 519
- Tolstoy, E., Saha, A., Hoessel, J. G., & McQuade, K. 1995, *AJ*, 110, 1640
- Tosi, M., Bellazzini, M., Aloisi, A., Greggio, L., Leitherer, C., & Montegriffo, P. 2001, *AJ*, 122, 1271
- Tully, R. B. 1988, *Nearby Galaxies Catalog* (Cambridge: Cambridge Univ. Press)
- Vogler, A., & Pietsch, W. 1996, *A&A*, 311, 35
- Wang, D., et al. 2004, *ApJ*, 609, 113
- Winter, L. M., et al. 2005, *ApJ*, submitted
- Zdziarski, A. A., & Gierliński, M. 2004, *Prog. Theor. Phys. Suppl.*, 155, 99
- Zimmermann, H. U., & Aschenbach, B. 2003, *A&A*, 406, 969